

Faraday Discussions

Accepted Manuscript



This is an Accepted Manuscript, which has been through the Royal Society of Chemistry peer review process and has been accepted for publication.

Accepted Manuscripts are published online shortly after acceptance, before technical editing, formatting and proof reading. Using this free service, authors can make their results available to the community, in citable form, before we publish the edited article. We will replace this Accepted Manuscript with the edited and formatted Advance Article as soon as it is available.

You can find more information about Accepted Manuscripts in the [Information for Authors](#).

Please note that technical editing may introduce minor changes to the text and/or graphics, which may alter content. The journal's standard [Terms & Conditions](#) and the [Ethical guidelines](#) still apply. In no event shall the Royal Society of Chemistry be held responsible for any errors or omissions in this Accepted Manuscript or any consequences arising from the use of any information it contains.

This article can be cited before page numbers have been issued, to do this please use: G. Barber, X. Chen, A. Khan, J. Heinlein, S. M. Gericke, M. Li, D. Zakharov, J. C. Yang, A. Head, M. Cargnello, R. M. Rioux and S. R. Bare, *Faraday Discuss.*, 2026, DOI: 10.1039/D5FD00172B.

The Ever-Evolving Active Site: Transformation of Single Atoms to Extended Structures during Rh-catalyzed Reverse Water-Gas Shift Reaction

Greg Barber^{a,§}, Xiaobo Chen^{b,c,§}, Anastassiya Khan^d, Jake Heinlein^e, Sabrina M. Gericke^b, Meng Li^b, Dmitri Zakharov^b, Judith Yang^{b,c}, Ashley R. Head^b, Matteo Cargnello^e, Robert M. Rioux^{a,f}, Simon R Bare^d

^a Department of Chemical Engineering, Pennsylvania State University, University Park, Pennsylvania, 16802, United States

^b Center for Functional Nanomaterials, Brookhaven National Laboratory, Upton, New York 11973, United States

^c Department of Chemical and Petroleum Engineering, University of Pittsburgh, Pittsburgh, Pennsylvania 15261, United States

^d SSRL, SLAC National Accelerator Laboratory, Menlo Park, California, 94025, United States

^e Department of Chemical Engineering, Stanford University, Stanford, California 94305, United States

^f Department of Chemistry, Pennsylvania State University, University Park, Pennsylvania 16802, United States

[§]These authors contributed equally to the work

Abstract. At low temperatures (< 400°C), single atoms of Rh supported on rutile TiO₂ (rTiO₂) are responsible for the formation of CO during the reverse water gas shift (RWGS), while methane production is associated with the Rh-TiO₂ interface due to the observed correlation between methane formation rates and the volume-averaged Rh nanoparticle diameter. As the temperature is increased to >540°C, there is a notable increase in CO selectivity as the methane production rates tend towards zero. The time to reach zero depends on the temperature but is independent of the initial Rh structure (single atoms and/or nanoparticles), which is controlled by the catalyst preparation method (wetness impregnation versus colloidal nanoparticles). At 600°C and > 4 h time on stream, the catalytic behaviour becomes completely agnostic to the



initial Rh structure as well as weight loading, and the catalysts are highly selective for the RWGS reaction. Post-reaction HR-TEM image analysis confirms Rh nanoparticles crystallize/order during the reaction; at 400°C, most of the Rh particles are disordered, while at 600°C, they are more ordered (i.e., development of defined faceting). Infrared spectroscopy of CO adsorption on Rh nanoparticles confirms the appearance of defined facets after annealing in nitrogen at high temperatures. Annealing the Rh/rTiO₂ catalysts prior to the RWGS reaction demonstrates the structural transformation of Rh depends only on time and temperature and not on reactant or product fugacity. Sites responsible for stabilizing Rh single atoms are no longer competent at higher temperatures, enabling single atom integration into existent nanoparticles. As the reaction temperature is increased to temperatures >540°C, the dominant Rh structure for CO production evolves from single atoms to extended surfaces.

1. Introduction

The reverse water gas shift reaction, (RWGS, $\text{CO}_2 + \text{H}_2 \rightarrow \text{CO} + \text{H}_2\text{O}$) is an industrially relevant reaction to produce carbon monoxide (CO) from carbon dioxide (CO₂) and hydrogen (H₂). This reaction has been discussed as a central component in the so-called power to liquids scenario where water electrolysis is used to make H₂, RWGS converts this H₂ and CO₂ to CO, and then the resulting syngas is converted into liquid fuels using Fischer-Tropsch catalysis.^{1–3} One of the most significant challenges with the RWGS reaction is selectivity to CO due to the competing Sabatier reaction, $\text{CO}_2 + 4\text{H}_2 \rightarrow \text{CH}_4 + 2\text{H}_2\text{O}$. This reaction is heavily exothermic (-165 kJ/mol), while RWGS is endothermic (41.5 kJ/mol).



Therefore, the RWGS presents fundamental selectivity challenges. If a catalyst is unselective for RWGS versus methanation, then the product distribution is dictated solely by thermodynamics and high temperatures ($\geq 600^\circ\text{C}$) are required to suppress CH_4 formation and achieve high CO yield. Such high temperatures typically promote sintering of the dispersed active phase of the catalyst. If a catalyst kinetically controls CH_4 formation, then substantial CO selectivity is possible at lower temperatures. Most heterogeneous catalysts for RWGS utilize transition metals or oxides as the active species, which are deposited on high surface area oxide supports.⁴ Interestingly, it has been found when Ni, Ru, and Rh supported catalysts are synthesized to promote the formation of atomically dispersed or single atom metal species, as opposed to metal nanoparticles (NPs), they are highly selective for RWGS⁵⁻⁹. These studies support the notion that provided the active metal can be stabilized in the form of single atoms, there are opportunities to perform RWGS at lower temperatures due to the high selectivity of the single atoms at lower temperatures. However, because of RWGS thermodynamics, operation at high temperatures is mandatory. For example, at 400°C , for 3:1 H_2/CO_2 mixture, the equilibrium conversion is only 38.1%, it increases to 51.9% at 500°C and is 63.1% at 600°C (the highest temperature explored in this manuscript). Moreover, the literature teaches that regardless of whether thermodynamics are used to control RWGS selectivity by operating at very high temperatures, or kinetics are used to control selectivity by operating at low temperature using atomically dispersed metal catalysts, sintering of the active metal domains must be suppressed to promote long term catalyst stability.

As such we have explored the use of Rh/rTiO_2 for the RWGS reaction. Earlier work using atomically dispersed Rh/TiO_2 (P25) demonstrated isolated atoms and nanoparticles of the same



metal on the same support can exhibit uniquely different catalytic selectivity in competing reaction pathways at a reaction temperature of 200°C and low conversion conditions⁵. Moreover, dispersion of nanoparticles under reaction conditions can play a significant role in controlling stability.⁵ More recently, under high conversion conditions with Rh/rTiO₂, it was demonstrated the product selectivity is governed by the evolving distribution of Rh moieties under reaction conditions: the balance between Rh single atoms and Rh nanoparticle–TiO₂ interfacial sites determines CO versus CH₄ formation. Moreover, it appeared Rh single atoms are unexpectedly robust over at least 90 h on stream at 500°C, even at high Rh density, whereas Rh NPs sinter.¹⁰ Additionally, we reported the results of a round robin study of Rh/rTiO₂ catalysts for RWGS across four laboratories¹¹, where the time-dependent production rates of CO via RWGS and CH₄ via methanation were measured at an appreciable approach to equilibrium. In this study the CH₄ formation rate rapidly decreased between 500°C and 600°C for higher Rh weight loadings. These studies indicate the reaction temperature plays an important role in the type and stability of the Rh structures present on the titania, motivating the current study.

In this work we report on the evolution of the reactivity and structure of a series of Rh/rTiO₂ catalysts under RWGS conditions at high conversions (400–600°C, 1 atm, 75% H₂, 25% CO₂) as a function of time on stream (16 h). A series of rutile-supported catalysts were prepared by both wetness impregnation (WI) and colloidal synthesis (CS/NP) with nominal weight loadings ranging from 0.1 to 2 wt. % Rh. The catalysts were characterized using transmission electron microscopy (TEM), CO diffuse reflectance infrared spectroscopy (CO DRIFTS), and X-ray photoelectron spectroscopy (XPS). We show irrespective of both the catalyst preparation method and the Rh weight loading, all catalysts operated at 600°C exhibit similar selectivity to CO (>98%) after



prolonged (16 h) time on stream. TEM analysis after reaction for 16 h show a similar mean Rh nanoparticle size among all catalysts. We show pre-treatment in an inert gas (annealing) prior to the RWGS reaction significantly improves the initial CO selectivity. We attribute these observations to a change in the ordering/crystallinity of the Rh NPs, which enables the establishment of new active sites for CO production. This work clearly demonstrates at temperatures $>500^{\circ}\text{C}$, evolution of the Rh structure requires only time and temperature; the details of the CO_2 hydrogenation atmosphere is not a prerequisite for Rh restructuring.

2. Methods

2.1 Catalyst synthesis

2.1.1 Synthesis of wet impregnation catalysts

Rhodium-supported rTiO_2 (Rh/ rTiO_2) catalysts with nominal Rh loadings of 0.1, 0.3, and 2 wt. % were prepared via wet impregnation (WI), following a previously reported procedure.¹¹ Briefly, Rh(III) nitrate hydrate (Sigma-Aldrich, $\sim 36\%$ Rh) was dissolved in HPLC-grade water and added to a suspension of rTiO_2 (US-Nano, 99.9%, 30 nm particle size) prepared at 12 g TiO_2 per liter. The Rh precursor solution was fed at 0.5 mL/min with a syringe pump, after which the water was evaporated at 100°C . The resulting solids were dried overnight at 100°C , ground, and calcined under dry air at 400°C for 4 h with a ramp rate of $10^{\circ}\text{C}/\text{min}$. These catalysts are referred to as wetness impregnated (WI) catalysts, with the designation X wt. % Rh/ rTiO_2 (WI).

2.1.2 Synthesis of colloidal Rh nanoparticles (NPs)

Rhodium nanoparticles (Rh NPs) were synthesized based on previous work.¹² Briefly, RhCl_3 (Sigma-Aldrich, 41.8 mg), polyvinylpyrrolidone (PVP) (Sigma-Aldrich, 222 mg, MW = 55,000), glucose (Sigma-Aldrich, 720 mg), and KBr (Sigma-Aldrich, 71.4 mg) were dissolved in 10 mL of



water and added to a pressure flask (Ace Glass Inc.). The flask was sealed and heated to 140°C under magnetic stirring for 3 h. The nanoparticles were then washed in water and separated via precipitation with acetone three times before being dispersed and stored in water. Thermogravimetric analysis (TGA) was performed to determine the Rh NP concentration in the solution.

2.1.3 Deposition of the Rh NPs

The Rh NPs were supported on rTiO₂ support following an antisolvent-induced adsorption method. Typically, rTiO₂ (500 mg) was dispersed in water (5 mL) and sonicated for 5 min. The Rh NP solution (volume calculated to achieve desired weight loading) was then added under magnetic stirring for 5 min. Acetone was then added dropwise until precipitation occurred (final acetone:water ~3:1, v/v). The precipitate was then collected and dried in an oven overnight at 80°C. The sample was then sieved below 180 μm grain size and calcined at 500°C for 3 h to remove the organic ligands. Removal of the PVP ligands was ensured by conducting temperature programmed oxidation (Fig. S1) and XPS (Fig. S2). All chemicals were purchased from Sigma-Aldrich and the rTiO₂ was purchased from US-Nano (US-Nano, 99.9%, 30 nm particle size). These catalysts are referred to as colloidal synthesis nanoparticle CS/NP catalysts, with the designation X wt. % Rh/rTiO₂ (CS/NP).

2.1.4 Catalyst testing

A full description of the reactor used in this study is presented elsewhere.¹¹ Briefly, two identical packed-bed reactors share a common gas supply (H₂ (99.9999%), CO₂ (99.999%), O₂ (20% in N₂, UHP), and N₂ (UHP), Linde Praxair) which is directed through Silcolloy 2000-coated stainless lines and split into individual manifolds of thermal mass flow controllers (MFCs). The gases from each



MFC were mixed downstream and passed through a 50 mL Silcolloy-2000 coated stainless preheater packed with 30-mesh SiC at 200°C before entering Silcolloy-coated stainless steel reactor tube (9.5 mm OD, 7 mm ID, 300 mm length). The temperature of the reactor was controlled with a clamshell furnace (Applied Test Systems, Butler, PA) using a K-type thermocouple (DwyerOmega, Michigan City, IN) inserted directly in the bed and a second K-type contacted the reactor tube wall. Reactor operations were controlled via LabView. The exhaust was maintained at ambient temperature and pressure to condense water and fix the water vapor pressure prior to gas chromatography analysis. Products (CO₂, CH₄, CO) were quantified by gas chromatography (Shimadzu 2030) with an Rt-Q-Bond PLOT column (Restek Corporation, Bellefonte, PA, 30 m, 0.53 mm ID × 20 mm). Nitrogen was used as a carrier gas and an FID with a methanizer was used for gas quantification. The initial catalytic testing of the catalysts followed a prior procedure.¹¹ In this study, we used Rh/rTiO₂ catalysts with variable weight loading (0.1 - 2 wt. % nominal). All reactions were conducted with a total of 20 μg of Rh; the total catalyst amount varied for each catalyst (20 mg for 0.1 wt. %, 6.7 mg for 0.3 wt. %, 1.0 mg for 2.0 wt. % total Rh loading) unless otherwise noted. This mass of catalyst was then Vortex mixed with nominally 500 mg of SiO₂ diluent (Product 84878, MilliporeSigma) for 15 s before being formed into a packed bed on top of a quartz wool support bed inside the reactor tube. The catalyst bed height was standardized within the furnace's uniform temperature zone by compressing 88 ± 3 mg quartz wool into the tube bottom and using a fixed length mounting jig to set the distance of the quartz wool support bed from the bottom of the reactor tube.

The reaction environment and thermal profile as a function of time for a representative sample is illustrated in Fig. 1a. The overall protocol for reaction testing was (i) purge reactor tube



with 20 sccm of nitrogen (N₂, UHP, Linde Praxair) and 100 sccm of 20% O₂ in N₂ (balance) (UHP grade, Linde Praxair), (ii) oxidation at 400°C for 30 min (10°C/min ramp rate) under 20% O₂ in N₂ (balance) at 32 sccm, (iii) cool catalyst down to < 40°C under same gas flow in (iii), (iv) purge the system of oxygen with N₂ (UHP, Linde Praxair) at 20 sccm for 25 min, (v) switch to 3:1 ratio H₂:CO₂ (H₂: 99.9999+%, CO₂: LaserStar5.0, 99.999%, Linde Praxair) at a total flow rate of 32 sccm for 30 min with the sample temperature < 40°C, and (vi) ramp the catalyst to reaction temperature at 10°C/min and hold for 16 h under same gas flow in (v). This procedure is referred throughout the manuscript as the normal/standard RWGS protocol (Fig. 1a).¹¹

For annealed catalyst samples, the preparation and the reaction protocol was identical through the post oxidation purge (step iv). After this step, the catalyst was reduced and annealed prior to exposure to the 3:1 H₂/CO₂ mixture. In these experiments, the Rh catalyst was reduced by exposing the sample at < 40 °C to 20% H₂ in N₂ (Linde, UHP grade), ramping at 10°C/min to 200°C and holding for 5 min under at a total flow rate of 25 sccm before purging the reactor with 20 sccm of N₂ (Linde, UHP) for 25 min. After the post reduction purge, the sample was heated to the annealing temperature at 10°C/min in 20 sccm of N₂ for a predetermined amount of time (from 1-2 h) prior to exposure to a 3:1 H₂:CO₂ mixture. A representative reaction environment and thermal profile for a sample annealed at 500°C for 2 h is shown in Fig. 1b. In Fig. 1a and 1b, the main reaction processes of oxidation, reduction, annealing, and under RWGS environment at reaction temperature are summarized. The relevant definition of elapsed time and time at reaction temperature are indicated in Fig. 1. Elapsed time is only shown to help guide the reader on the total time for the pre-treatments before collection of the catalytic data using 'time at reaction temperature.'



The CO₂ conversion (X_{CO_2}) and CO selectivity (S_{CO}) are defined as follows, where n_i denotes the moles of species i leaving the reactor:

$$X_{CO_2} = \frac{n_{CO} + n_{CH_4}}{n_{CO} + n_{CH_4} + n_{CO_2}}$$

$$S_{CO} = \frac{n_{CO}}{n_{CO} + n_{CH_4}}$$

The net production rates are defined as: “CO production rate” (and analogously “CH₄ production rate”) denotes CO (or CH₄) production rates (r_{CO}/r_{CH_4}) normalized per mole of total Rh. These are integral rates, rather than commonly used differential rates for turnover frequency (TOF) or space-time yield (STY) calculations and rate, r_i is defined as $r_i = \frac{F_i}{mol_{Rh}}$, where F_i is the molar flow rate of CO or CH₄ exiting the reactor and mol_{Rh} is the total moles of Rh in the rTiO₂ catalyst.

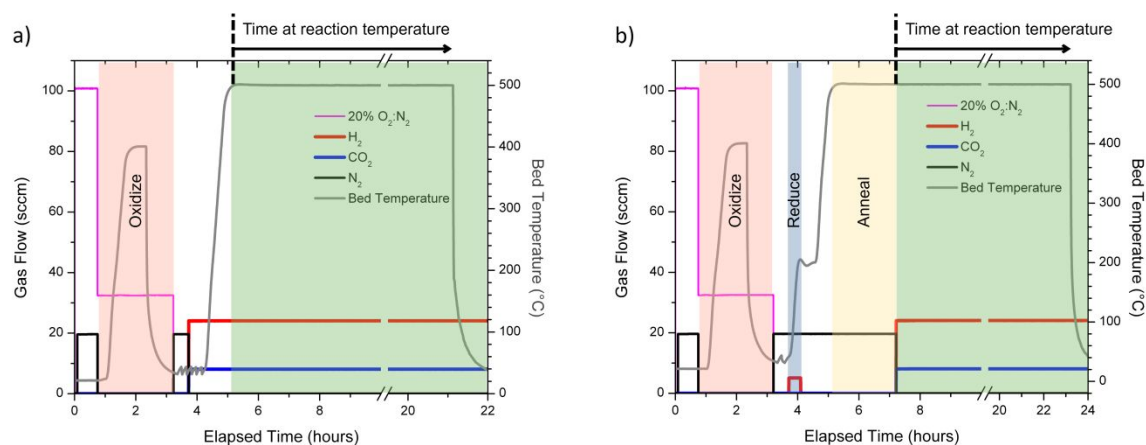


Figure 1. Representative reaction environments and thermal profiles for non-annealed samples with the standard protocol (a) and samples that undergo annealing (b) before being exposed to the same 3:1 H₂:CO₂ environment. In (b), the reduction step occurs at 200°C under 20% H₂ in N₂ after the post oxidation purge and prior to annealing under nitrogen and introduction of the RWGS gases. The main processes of purge, oxidation (light orange), reduction (light blue), annealing (light yellow), and time at which the sample is exposed to 3:1 H₂:CO₂ RWGS environment at reaction temperature (light green) are labelled.

2.2 Catalyst characterization



2.2.1 Inductively coupled plasma – optical emission spectroscopy (ICP-OES)

The ICP-determined wt. % Rh amounts (ICP-OES; Galbraith Laboratories) of the catalysts were 0.1 wt. % Rh/rTiO₂ (WI): 0.0993 wt. %, 0.3 wt. % Rh/rTiO₂ (WI): 0.277 wt. %, 2 wt. % Rh/rTiO₂ (WI): 1.6 wt. %, and 0.3 wt. % Rh/rTiO₂ (CS/NP): 0.230 wt. %. Throughout the manuscript we refer to each catalyst by their nominal loadings.

2.2.2 CO diffuse reflectance infrared Fourier transform spectroscopy (CO DRIFTS)

Catalyst samples were characterized by CO-DRIFTS using a high-temperature Harrick Reactor cell. This reactor cell was mounted inside a Thermo Scientific Praying Mantis diffuse reflectance adapter for a Nicolet iS50 FTIR Spectrometer. The reactor cell was heated by resistive cartridge heaters controlled by a PID temperature controller with a thermocouple positioned at the bottom of the catalyst bed for accurate temperature readings. Most of the sample cup was filled with Al₂O₃ powder (50 nm particle size), topped with a thin, flat layer of Rh/rTiO₂ catalyst.

All samples were pretreated in situ in 20% O₂/He at 400°C for 30 min (ramp 10°C/min) and then cooled to room temperature in the same O₂ flow. After purging with He, the samples were reduced in 20% H₂/He at 200°C for 5 min (ramp 10°C/min), followed by a 20 min He purge to remove residual hydrogen. Subsequently, the samples were heated in He to the desired annealing temperature (400, 500, or 575°C) at a rate of 10°C/min and held for the specified dwell time (30 min, 1 h, or 2 h). The temperature (575°C) represents the highest temperature the Harrick reactor cell was able to reach. After cooling to room temperature, a background spectrum was collected. The samples were then exposed to 10% CO/Ar (UHP, Airgas) at room temperature until the CO adsorption reached saturation coverage, after which gas-phase CO was



purged with He for 45 min until all gas phase CO signatures disappeared and the final CO-DRIFTS spectrum was then recorded.

Peak deconvolution was done using OMNIC software with Voigt functions. Peak heights were allowed to be in the range of 0-10 absorbance units, Gaussian full width at half heights were allowed to be in the range of 0-32 cm^{-1} , and Lorentzian widths were allowed to be in the range of 0-450 cm^{-1} . The noise was set to 0.05 and a baseline was not used. The initial number of peaks was determined using the peak finder with low sensitivity to reduce overestimation of the number of peaks. The number of peaks was increased until the fit was constant and the fit parameter no longer decreased.

2.2.3 *Transmission electron microscopy (TEM)*

TEM characterization was performed using an objective-lens aberration-corrected transmission electron microscope (FEI Titan 80–300) at the Center for Functional Nanomaterials, Brookhaven National Laboratory (Upton, NY). The microscope was operated at an accelerating voltage of 300 kV, with a spatial resolution of 0.8 Å in the high-resolution TEM (HRTEM) mode. Post-reaction samples were deposited onto TEM grids after gently shaking the container containing both the sample and TEM Cu grid, enabling the particles to disperse onto the grid. All TEM images were acquired with a 0.5 s exposure at a “safe illumination” dose rate, as defined by continuous exposure experiments (Fig. S3) and consistent with the imaging protocol in our previous work¹³ ImageJ was used to measure the diameter of the Rh NPs, with each size distribution derived from more than 400 particles. Potential Rh single atoms and ultra-small clusters were not included in the HRTEM-based size distribution analysis because their weak atomic contrast is overwhelmed by the strong scattering from the TiO_2 support. The evaluation of ordered versus disordered



structure was carried out using Fast Fourier Transform (FFT) analysis of the HRTEM images of Rh NPs. Only edge-on Rh particles acquired under appropriate defocus conditions were included to avoid artifacts arising from support-induced reduction in the signal-to-noise ratio. We classified NPs as ordered when sharp diffraction spots appeared in their FFTs; in the absence of such spots, they were categorized as disordered. The absence of lattice fringes and sharp diffraction spots in small crystalline Rh NPs may result from defocus, off-axis orientation, or electron-beam-irradiation-induced damage, and these factors were carefully considered to avoid misinterpretation.

2.2.4 Ambient pressure X-ray photoemission spectroscopy (AP-XPS)

Ambient-pressure XPS (APXPS) measurements were performed at the Center for Functional Nanomaterials (CFN) at Brookhaven National Laboratory (Upton, NY).¹⁴ The system consists of a SPECS PHI OBOS 150 NAP hemispherical analyzer in combination with a monochromatic Al K α X-ray source (1486.6 eV, \sim 0.25 eV line width), focused to a spot size below 300 μ m. To reduce charging, the catalyst powder was lightly pressed onto a tantalum (Ta) foil to enhance electrical conductivity. The Ta foil with the catalyst was then mounted directly onto the sample holder via spotwelding. The Rh 3d spectra were energy calibrated by aligning the Ti2p_{3/2} peak of the TiO₂ support to 459.3 eV to account for minor support charging effects. The spectra were fitted using CasaXPS. A Shirley background was subtracted from the spectra.

3. Results and Discussion

3.1 Methane Selectivity decreases with Reaction Temperatures > 500°C



We explored the impact of reaction temperature ($>500^{\circ}\text{C}$) on CO selectivity for Rh/rTiO₂ catalysts produced by two distinct methods (WI and CS/NP) containing both Rh single atoms and nanoparticles ($d < 4.5$ nm). Figure 2 summarizes CO and CH₄ net production rates at reaction temperatures between 500–580 $^{\circ}\text{C}$ for 0.3 wt. % Rh/rTiO₂ (WI) catalysts over 16 h. In a recent round robin study,¹¹ the 0.3 wt. % Rh/rTiO₂ had the highest CH₄ production rate at 500 $^{\circ}\text{C}$ of all examined Rh/rTiO₂; therefore, it was chosen as the initial catalyst to examine the impact of temperature above 500 $^{\circ}\text{C}$ on the production of CH₄. Figure 2a clearly demonstrates CO net production rates increase with temperature and remain relatively constant over 16 h. Duplicate measurements at 540 $^{\circ}\text{C}$ and 560 $^{\circ}\text{C}$ demonstrate reproducible behavior between the experiments conducted on two separate diluted catalyst beds. The fate of CH₄ production rates with time on stream follows very different behavior. At 500 $^{\circ}\text{C}$ (black data), the CH₄ production rate continually decreases over the 16 h experimental window at a rate of CH₄ loss of 0.1–0.2 mol/mol_{Rh}/s per hour. Similar temporal behavior in the decline of CH₄ production rates is observed at 540 $^{\circ}\text{C}$, and a duplicate catalyst bed demonstrates a similar temporal trend. At 560 $^{\circ}\text{C}$, the rate of methane production decreases at an average rate of CH₄ loss of 0.56 mol/mol_{Rh}/s per hour and is < 1 mol/mol_{Rh}/s at 16 h. At 580 $^{\circ}\text{C}$, the rate of methane production decreases at ~ 1.3 mol/mol_{Rh}/s per hour and reaches 1 mol/mol_{Rh}/s after only 6 h, which corresponds a 60% reduction in time compared with a reaction temperature of 560 $^{\circ}\text{C}$. Over the same temperature window, the rate of CO production is rather constant and only increases by more than 10% for the samples at 560 $^{\circ}\text{C}$. The disparate behavior with temperature and time-on-stream between CO and CH₄ production rates implies a loss of active sites associated with CH₄ formation while the active sites associated with CO formation appear resilient, ultimately



suggesting these products are produced on unique sites. These CO-resilient sites could be associated with our prior study where Rh single atoms exhibited stability for the duration of 90 h reactivity measurements. This prior study was conducted at a reaction temperature of 500°C, which is substantially below the onset of the behavior discussed here. Utilizing the time-on-stream production rates, the CO selectivity is greater than 97% at 580°C for time at reaction temperature greater than 8 h.

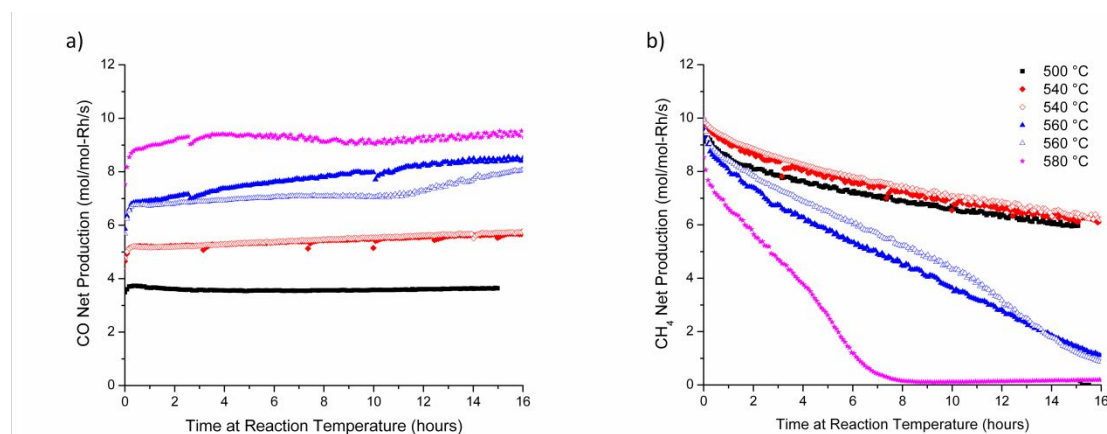


Figure 2. CO (a) and CH₄ (b) net production rates as a function of temperature for 0.3 wt. % Rh/rTiO₂ (WI). CO net production rates increase with increasing temperature and are stable with time-on-stream. Initial CH₄ production rates do not follow the same trend with temperature and decrease with increasing time on stream. The methane production rate decreases significantly for temperatures greater than 540°C. The RWGS reaction at 540 and 560°C were conducted in duplicate (open symbols) to demonstrate reactor reproducibility.

3.2 Methane selectivity at 600°C is agnostic to the initial Rh structure

To determine if these observations of decreasing CH₄ net production rate with temperature in excess of 560°C were not limited solely to the 0.3 wt. % Rh/rTiO₂ (WI) catalyst, additional rutile-supported Rh catalysts (0.1 wt. % Rh/rTiO₂ (WI), 2 wt. % Rh/rTiO₂ (WI), and 0.3



wt. % Rh/rTiO₂ (CS/NP)) were tested under the standard RWGS protocol (Fig. 1a) at a temperature of 600°C for 16 h. Fig. 3 summarizes the CO net production rate (Fig. 3a) and CH₄ net production rate (Fig. 3b) for all catalysts tested. The CO net production rate (Fig. 3a) shows a general trend of constant CO production with time greater than 6-8 h on stream after a 0-30% decrease in initial CO production rates over the first several hours. WI catalysts consistently demonstrate higher CO production rates than CS/NP catalysts. The CH₄ production rates in Figure 3b demonstrate all rutile-supported Rh catalysts exhibit 20-100× lower CH₄ production than CO production at 600°C regardless of Rh weight loading and preparation method. This rapid decrease in CH₄ production during the first several hours on stream coupled with the much more constant CO production rates, and increased CO selectivity before reaching their maximum CO selectivity within 4 h of reaching 600°C. There is a slow decrease in CO selectivity after the maximum, but this is not due to a decrease in CO production rate but is due to the slow increase in the CH₄ production rate (Fig. 3b). This behavior in CH₄ net production rates is also seen in Figure 2b for the 0.3 wt. % Rh/rTiO₂ (WI) sample at 580°C suggesting this phenomenon is not limited to a temperature of 600°C. As with data in Fig. 2, several weight loadings and catalyst preparation methods were run in duplicate to demonstrate the reproducibility with time on stream trends across different catalyst beds; all duplicate runs are noted with open symbols in Fig. 3a-b.



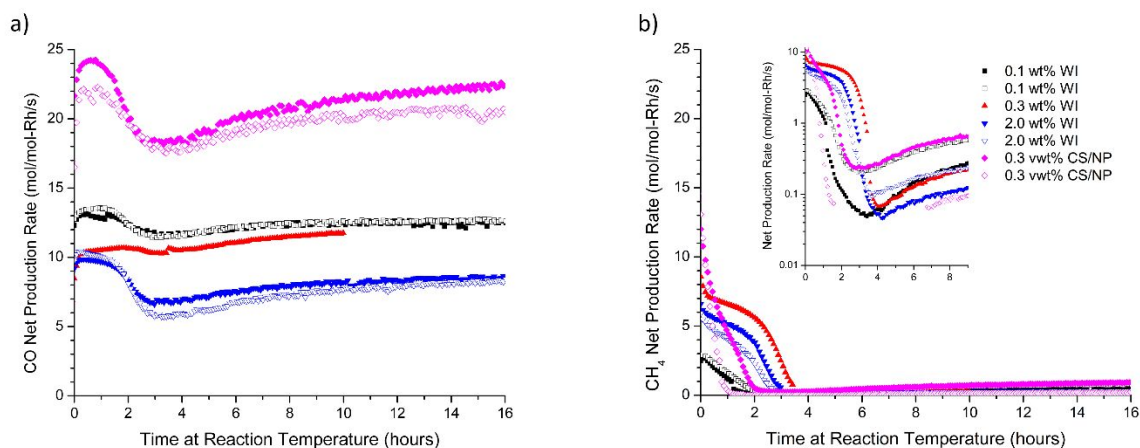


Figure 3 – (a) CO net production rates and (b) CH₄ net production rates for all Rh/rTiO₂ catalysts exposed to standard RWGS procedure and a reaction temperature of 600°C. A general trend of constant CO production rate with time-on-stream regardless of Rh weight loadings and preparation method is observable in (a) while (b) shows all Rh/rTiO₂ catalysts have very low CH₄ production rates (typically 0.1-0.5 mol/mol-Rh/s) at 600°C regardless of Rh weight loading and preparation method. Duplicated reaction conditions are represented by open symbols.

3.3 Ex-situ TEM characterization of catalysts after reaction displays final particle size distribution

Ex-situ TEM characterization was conducted on the post-reaction Rh/rTiO₂ catalysts with Rh loadings of 0.1, 0.3, and 2.0 wt. % following standard RWGS reaction conditions at 400°C, 500°C, and 600°C for 16 h. Catalytic performance data for the samples tested at 400°C and 500°C are the same as reported previously.¹¹

For the 0.1 wt. % Rh/rTiO₂ (WI) catalyst, a predominantly single atom catalyst in the fresh state (see Fig. S3)¹⁰, the TEM image (Fig. 4a) after RWGS reaction at 400°C reveals the formation of discrete Rh NPs, indicating reaction-induced sintering. The particle-size distribution (Fig. 4b) is relatively uniform, with an average diameter of ~1.8 nm. The 2.0 wt. % Rh/rTiO₂ (WI) (Figs. 4(c,d)) exhibits a similar mean particle size as the 0.1 wt. % catalyst even though it has an order of



magnitude higher loading of Rh. The comparable size across catalysts with different Rh loadings after RWGS at 400°C regardless of weight loading suggests thermodynamic factors dominate reaction-induced restructuring.^{15,16}

The 0.1 wt. % catalyst (Figs. 4(e,f)) post reaction at 500°C exhibits a size distribution comparable to the same catalyst post reaction at 400°C, whereas the 2.0 wt. % catalyst (Figs. 4(g,h)) shows a broader size distribution but a similar mean size. Furthermore, the 0.1 wt. % catalyst post reaction at 600°C maintains a nearly identical mean particle size (~1.8 nm) and narrow size distribution (Figs. 4(i,j)), consistent with large interparticle spacing suppressing particle coalescence at low loading.¹⁷ For the higher-loading catalysts (0.3 and 2.0 wt. %) post reaction at 600°C shown in Figs. 4(k-n), the mean particle size increases from 1.9 nm to 2.1 nm, respectively, along with a broader size distribution. To further investigate the sintering dynamics of post-reaction samples at different temperatures, the size distributions revealed low-loading samples (0.1 wt% and 0.3 wt%) maintain a narrow particle size distribution without the formation of large particles. In contrast, the 2 wt. % post-reaction samples exhibit an obvious increase in the fraction of sintering induced larger particles (6-10 nm) due to the shorter average distance between Rh species.¹⁰ Importantly, the population of large particles (6-10 nm) remains a minor contribution, less than 2% as shown in Fig. 4. For the 600°C post-reaction, 0.3 wt.% Rh/rTiO₂ (CS/NP) catalyst, TEM imaging (Figs. 4(o,p)) reveals unexpected particle shrinkage after reaction, relative to the fresh sample (see Fig. S3), possibly arising from fragmentation during catalytic reaction.^{18,19} Surprisingly, the post-reaction particle size distributions after RWGS at 600°C remain relatively consistent across samples with different loadings (0.1-2.0 wt. % Rh) and initial



Rh structures (WI or CS/NP), suggesting the final particle size is controlled by a thermodynamic equilibrium between sintering and fragmentation.

3.4 Differences in internal particle order post RWGS reaction

While the number of particles sampled by TEM imaging is small compared to the total number of particles present in each catalyst, the changes in particle size at the different reaction temperatures do not explain the time-dependent trends in CH₄ production rate and selectivity. A prior study of the RWGS conducted at 500°C, concluded that Rh single atoms are responsible for CO formation, and Rh NPs harbour sites (assigned previously to Rh nanoparticle-TiO₂ interfacial sites) are responsible for CH₄ production.¹⁰ Figure 3b clearly demonstrates the 0.1 wt. % Rh/rTiO₂ (WI) catalyst produces the least amount of methane on ramp to 600°C but ultimately has the lowest CO selectivity (albeit still > 90%) at 600°C and 16 h of reaction time. We previously postulated a population of Rh single atoms on rTiO₂ are stable at 500°C¹⁰; however, at 600°C, the appearance of Rh NPs with a mean diameter of ~1.8 nm suggests these Rh single atoms may no longer be stable. Fig. 3b further demonstrates CO selectivity is > 90% for all catalysts, regardless of the Rh weight loading and preparation method at 600°C, which differs from our recent round robin observations that both a 2 wt. % Rh/rTiO₂ (WI) or 0.3 wt. % Rh/rTiO₂ (CS/NP) at 500°C demonstrated a CH₄ selectivity of 15-20%.¹¹ Given our analysis demonstrated similar mean particle size after 16 h time-on-stream regardless of temperature (>400°C), we examined the particles further utilizing HRTEM imaging. Specifically, we sought to determine if structural differences in the supported particles could provide an explanation of the temperature dependent CH₄ selectivity.



HRTEM images and the corresponding fast Fourier transform (FFT) patterns in Fig. 5 illustrate structural differences between Rh/rTiO₂ after reaction at different temperatures. We chose to examine the 2.0 wt. % Rh/rTiO₂ (WI) since this sample had the highest particle density. HRTEM images of the catalyst post-reaction at 400°C (Figs. 5a and Fig. S5) shows disordered atomic arrangements and irregular nanoparticle morphologies, as further evidenced by the corresponding FFT pattern lacking sharp diffraction spots. Figs. 5b and S6 illustrates the HRTEM image of the post-reaction sample at 500°C contain well-arranged atomic columns, indicating increased structural ordering after reaction at higher temperature. The post-reaction samples at 600°C exhibit well-defined lattice fringes, faceted morphologies, and enhanced structural ordering, further confirming thermally promoted Rh crystallization under RWGS conditions (Fig. 5c). The crystallized Rh nanoparticles in Fig. 5(b,c) are the face-centered cubic (FCC) structure of metallic Rh. Fig. 5d quantifies the distribution of ordered and disordered Rh NPs at different temperatures. The results show an increase in the number of ordered Rh NPs with increasing reaction temperature. Most of the Rh NPs are well-ordered after reaction at 600°C, whereas a vast majority possesses defective or disordered structures at 400°C. It should be noted that the disappearance of lattice fringes in some Rh NPs classified as disordered may arise from slight defocus or off-axis orientation. In this study, we maintain such variations in slight defocus and orientation affect all samples similarly and therefore do not alter the observed temperature-dependent trend. However, the majority of Rh nanoparticles have characteristic sizes of approximately ~2 nm and therefore primarily govern the observed structural trends. Moreover, the in situ HRTEM images (Fig. S7) reveal dynamic structural evolution between disordered and ordered states during the RWGS reaction at 500°C. Overall, these temperature-dependent



structural variations under RWGS conditions suggest a dynamic restructuring processes that impact catalytic performance.

Moreover, the Rh NPs are crystallized/faceted with a similar particle size, as depicted in Figs. 5(e-h), illustrates the HRTEM images of the post-reaction samples at 600°C with different loadings and initial Rh preparation method (WI versus CS). Additional HRTEM images are depicted in Fig. S6. This structural consistency across sample preparation methods aligns with the temperature-dependent structural variations after RWGS, providing a potential explanation for the similar catalytic behaviour at 600°C and > 4 h time on stream. These results highlight the critical role of nanoparticle crystallinity in catalytic performance of Rh/rTiO₂ (WI) catalysts at 600°C. Fig. 5i shows Rh 3d XPS data that are consistent with the Rh being metallic post RWGS. The 600°C condition results in narrower peaks, supporting the more ordered Rh seen in the TEM results (additional discussion in Supplemental Information). Notably, no strong metal–support interaction (SMSI) overlayer was observed in TEM on any of the samples (400, 500, 600°C) studied. While Rh-TiO₂ interactions may contribute to nanoparticle stabilization to avoid long-distance particle migration.¹⁰ The lack of SMSI is further supported by XPS measurements, where the intensity ratio of Rh 3d to Ti 2p peaks is constant for the 400 and 600 °C samples, suggesting no overgrowth and Rh signal attenuation (Figure S9 and Section S3).



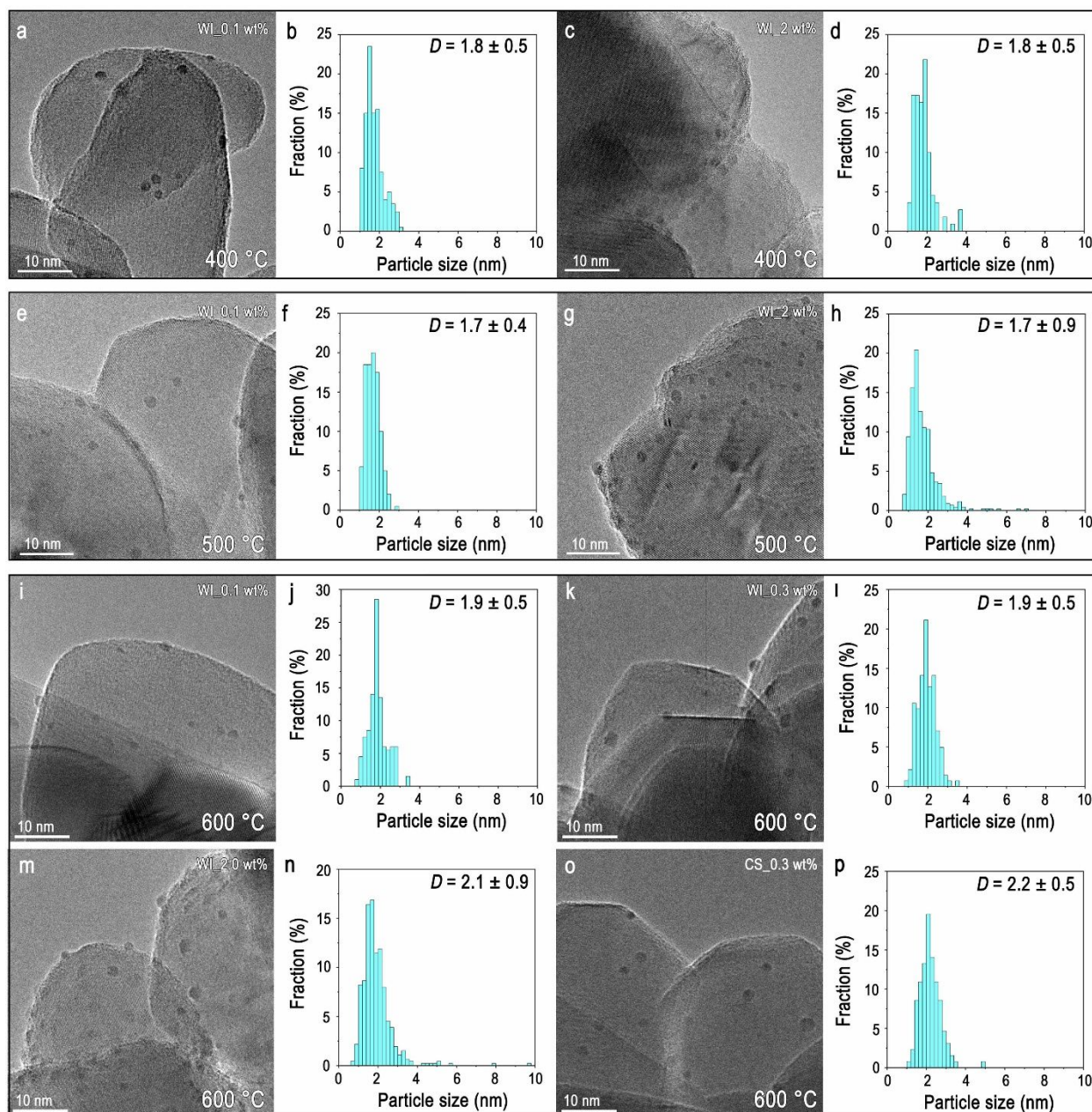


Figure 4. TEM characterization of the post-reaction samples subjected to the standard RWGS procedure at different temperatures. Low-magnification TEM images and corresponding particle size distributions are shown for the 0.1 and 2 wt. % Rh/rTiO₂ (WI) catalysts after 16 h of RWGS at 400°C (a-d), the 0.1 and 2 wt. % Rh catalysts after 16 h at 500°C (e-h), and for the 0.1, 0.3, 2 wt. % and 0.3 wt. % Rh (CS/NP) catalysts after 16 h at 600°C (i-p).



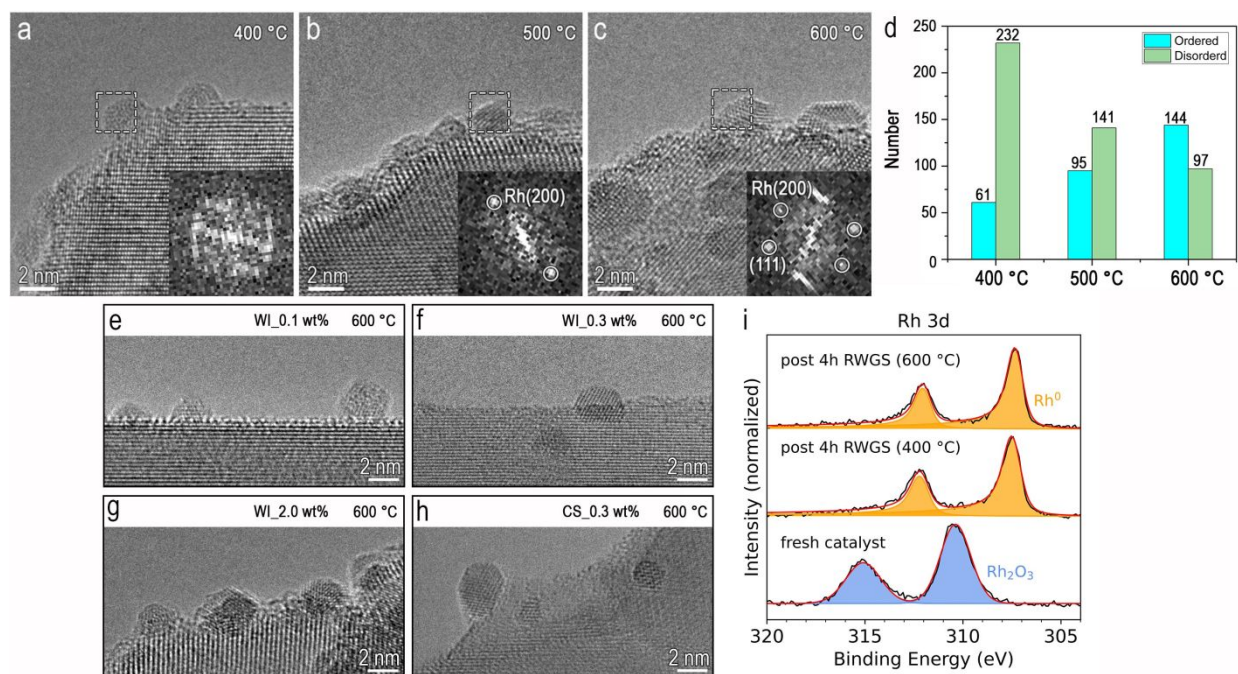


Figure 5. HRTEM imaging and structural analysis of the post-reaction samples exposed to the standard RWGS procedure at different temperatures. (a-c) HRTEM images of the 2 wt. % Rh/rTiO₂ (WI) catalyst after 16 h of RWGS at 400, 500, and 600 °C, respectively. Insets are the corresponding FFT images of the selected NPs highlighted by the dashed white rectangles. (d) Number of ordered versus disordered structures in the post-reaction samples as a function of reaction temperature. HRTEM imaging of post-reaction Rh/rTiO₂ catalysts at 600 °C with different loading: (e) 0.1 wt. % Rh (WI), (f) 0.3 wt. % Rh (WI), (g) 2 wt. % Rh (WI), and (h) 0.3 wt. % Rh (CS/NP), showing the well-crystallized and faceted Rh NPs. (i) *In situ* XPS measurements of the Rh 3d core level of the 2.0 wt.% WI catalysts show the fresh catalyst has oxidized Rh and the post-reaction Rh oxidation state is metallic.

3.5 Pre-reaction annealing of Rh/rTiO₂ in an inert atmosphere reduces transient formation of CH₄

Given the apparent lack of SMSI, we examined whether the ripening and ordering/crystallization of the Rh is induced by the reactive gases (CO₂, H₂, and RWGS products – CO and H₂O),



temperature, time, or a combination of these. To gain an understanding of the effect of temperature and time on the observed CO selectivity changes during the first several hours, we also examined the impact of an annealing step (i.e., heating metal catalyst in N₂ at a certain temperature and time) prior to the introduction of the 3:1 H₂/CO₂ mixture to the catalyst. For this investigation we chose the 0.3 wt. % Rh/rTiO₂ (CS/NP) catalyst, due to the expected structural changes it must undergo to wet the support, and the 2.0 wt. % Rh/rTiO₂ (WI) Rh, due to the propensity to produce nanoparticles and CH₄ in the earlier study.¹⁰

In these annealing experiments, after the oxidation pre-treatment, Rh/rTiO₂ catalysts were ramped at 10°C/min in 20% H₂ in N₂ to 200°C and held for 5 min. Following this reduction step the catalysts were directly heated at 10°C/min in N₂ to the stated annealing temperature and held for the appropriate time. After this step the catalyst was heated to the appropriate reaction temperature and the gas composition was changed to the 3:1 H₂/CO₂ mixture, as depicted in Fig 1b. It is evident from Figs. 2 and 3 that all major changes are in CH₄ production rate while CO production rate is rather constant with time. As a result, changes in CO₂ conversion and CO selectivity can be used as indicators of the trends in CH₄ production. Figures 6a and 6b show the CO₂ conversion and CO selectivity for 0.3 wt. % Rh/rTiO₂ (CS/NP) and Figure 6c and 6d are the CO₂ conversion and CO selectivity for 2.0 wt. % Rh/rTiO₂ (WI). Regardless of whether a catalyst was annealed or not, there are not large differences between that catalysts in the final CO₂ conversion and CO selectivity after 16 h. However, there are noticeable differences in the initial CO selectivity and the rate at which CO selectivity becomes constant with annealing time (Figs. 6(b, d)) at temperatures from 400-500°C. In particular, the 0.3 wt. % Rh/rTiO₂ (CS/NP) exhibits a rapid increase in initial CO selectivity as the annealing temperature is increased from



400°C to 500°C with a further dramatic increase in the initial CO selectivity to > 98% for an annealing treatment of 600°C for 1 h. There is also an increase in CO selectivity with increasing annealing temperature and time for the 2.0 wt. % WI catalyst, with the largest increase in CO selectivity being observed as the annealing temperature is again increased from 500°C to 600°C for the same 1 h duration. We attribute the different transient behavior in CO selectivity for $T < 600^\circ\text{C}$ for the CS/NP versus WI catalysts to their initial morphology. Particles present on fresh higher weight loading WI catalysts are raft-like (Fig. S4), indicative of favorable wetting behavior to the support, while the colloidal Rh NPs on the Rh/rTiO₂ (CS/NP) catalysts are nominally spherical and non-wetting on rTiO₂. Fig. 4 and Fig. 5 demonstrate after 16 h time on stream, the NPs formed in both catalysts are similar in size and shape. The restructuring of spherical Rh NPs ($d \sim 4.5$ nm) requires the movement of many more atoms to form faceted ~ 2 nm particles compared to the raft-like particles found in WI catalysts. This temporal difference in catalyst restructuring leads to the lag in improvement in CO selectivity for CS/NP catalysts.



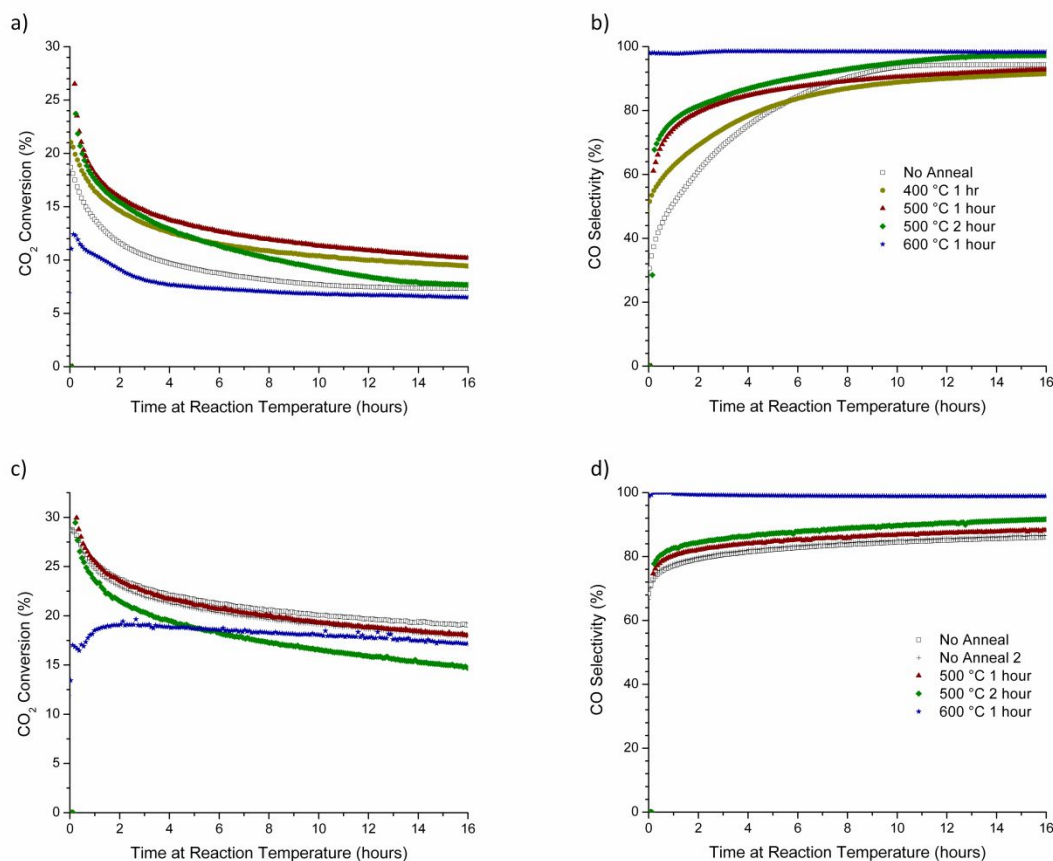


Figure 6. (a,c) CO₂ conversion and (b,d) CO selectivity for 0.3 wt. % Rh/rTiO₂ (CS/NP) (top) and 2 wt. % Rh/rTiO₂ (WI) (bottom) after annealing in nitrogen for variable times and temperatures. For each catalyst, the total CO₂ conversion appears independent of annealing conditions prior to the start of the RWGS reaction at 500°C under a 3:1 H₂:CO₂ environment. Annealing the catalyst prior to exposing to RWGS conditions improves the initial CO selectivity with more dramatic improvements observed for the 0.3 wt. % CS/NP catalyst than the 2.0 wt. % WI catalyst. CO selectivity increases with increasing temperature and time on stream for both catalyst types. For improved clarity, the repeat of the non-annealing reaction condition for the 2.0 wt. % WI catalyst is represented by the '+' sign.

3.6 Infrared spectroscopy of CO adsorption confirms defined Rh faceting after annealing

Figure 7 summarizes the observed CO DRIFTS spectra for three 0.3 wt. % Rh/rTiO₂ (CS/NP) catalysts after oxidation, reduction, and then annealing under He at various temperature/time



combinations prior to exposure to CO at room temperature. The samples were annealed at 400°C for 30 min (black), 500°C for 2 h (red), and 575°C for 2 h (blue). Since catalyst amounts varied between the CO DRIFTS experiments, only relative peak absorption intensities are used to compare results between different annealing conditions. However, peak intensities within each CO DRIFTS experiment can be used to define and compare relative contributions of different adsorbed CO configurations in each spectrum.

These CO DRIFTS absorption spectra are generally described by assigning the peak in the 1850-1970 cm^{-1} region to bridge bound CO on a Rh NP, the peaks at 2020 cm^{-1} and 2090-2100 cm^{-1} to the asymmetric and symmetric stretches of gem-dicarbonyl on rhodium single atoms and the peak in the 2040-2070 cm^{-1} region due to linear bound carbonyls on Rh NPs.²⁰⁻²² Detailed consideration of infrared absorption studies of CO adsorption on Rh single crystal surfaces may provide more insight regarding the evolution of the different Rh crystal facets as a function of annealing condition. We emphasize Rh single crystal studies are free of interference from gem dicarbonyl absorption due to their absence on extended low-energy Rh surfaces. Further, exact CO absorption peak frequencies and intensities depend on the surface coverage of CO (θ_{CO}) on each crystal facet.



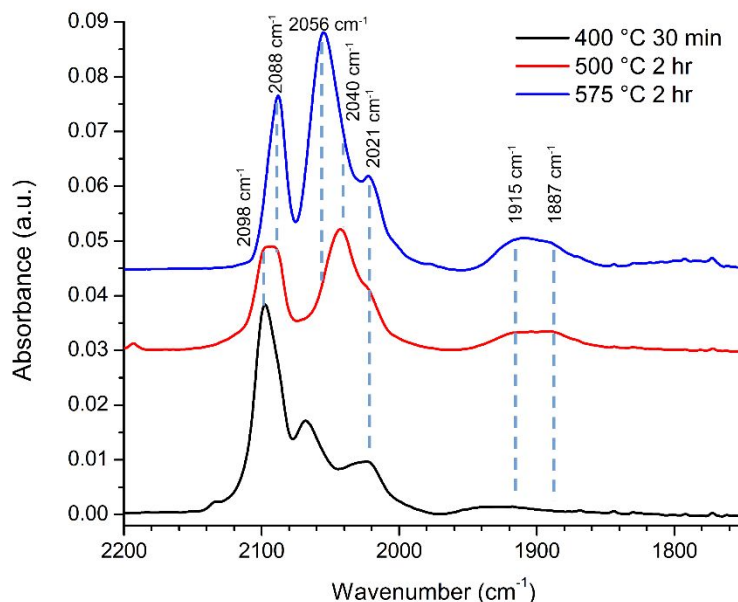


Figure 7. Infrared spectra of CO adsorbed at room temperature under a He purge on a 0.3 wt. % Rh/rTiO₂ (CS/NP) catalyst after annealing at 400°C for 30 min (black), 500°C for 2 h (red), and 575°C for 2 h (blue). The spectra were offset vertically. Vertical dashed lines are added to aid the eye and come from peak positions found through spectra deconvolution (see section S3). All deconvoluted spectra were assigned to specific absorption coverages on Rh crystal facets or for single atoms based on prior literature assignments for CO adsorption. Default fit parameters were used in the software with no forcings of peaks to be at any specific frequency or intensity.

The FTIR spectra in Fig. 7 clearly show changes in CO binding configuration as a function of annealing condition. To better understand the influence of annealing temperature each spectrum was deconvoluted. The results this peak deconvolution for the annealed catalysts in Fig. 7 are shown in Table 1. Full detailed peak deconvolution and fitting parameters are listed in Table S1-3 while the fits are shown in Supplementary Fig. S10-S12. The deconvoluted peaks in



Table 1 show that overall, the frequencies of the deconvoluted peaks were invariant in frequency and only changed in intensity with annealing conditions further supporting the idea that NPs and their final morphology evolve with time and temperature.

Table 1. List of deconvoluted peaks from OMNIC using default peak fit parameters and Voigt functions. The vibrational frequencies for the bridged and corresponding linear configurations that are observable at known surface coverages of CO on different Rh surfaces as well as vibrational frequencies for the gem-dicarbonyls on single atoms are color coded for clearer matching.

575 °C for 2 h	500 °C for 2 h	400 °C for 0.5 h	
Wavenumber (cm ⁻¹)	Wavenumber (cm ⁻¹)	Wavenumber (cm ⁻¹)	Peak Assignment
	2097.9	2098.8	Rh(CO) ₂ symm
2088.9	2087.9	2088.4	Rh(111)-O linear
	2069.6	2067.8	0.9-1.5 nm Rh NP linear
2056.7		2054.8	Rh(111) linear Rh(100) linear q = 0.50+ ML
2041.5	2043.5	2039.7	Rh(100) linear q = 0.35-0.40 ML
2021.1	2021.5	2022.4	Rh(100) linear q = 0.20 ML Rh(CO) ₂ asymm
2001.3			Rh(100) linear
		1940.1	Rh(100) bridge q > 0.50 ML
1912.6	1918.7	1912.9	Rh(100) bridge q = 0.35-0.40 ML
1885.3	1888.9		Rh(100) bridge q = 0.20 ML
		1869.7	0.9-1.5 nm Rh NP bridge



The deconvoluted peak data in Table 1 show a total of 11 different absorption peaks can be observed over the 3 different annealing conditions with 4 peaks assignable to CO in a bridging configuration on Rh surfaces (1870-1940 cm^{-1}), 6 peaks assignable to linear CO on Rh surfaces and/or the asymmetric stretch of Rh single atoms (2001-2088 cm^{-1}), and 1 peak associated with the symmetric stretch of Rh single atom signatures ($> 2090 \text{ cm}^{-1}$).²⁰⁻³⁴ All deconvoluted peaks contained shifts of $< \pm 1 \text{ cm}^{-1}$ except the low frequency bridging and the peak at 2041 cm^{-1} which shifted by $\pm 3 \text{ cm}^{-1}$ and $\pm 2 \text{ cm}^{-1}$ respectively. Of these peaks, only 3 (2021, 2056, and 2088 cm^{-1}) can be interpreted as multiple possible CO configurations belonging to either vibrations on multiple Rh crystal surfaces (2056 cm^{-1}) or Rh surfaces and single atoms (2021 and 2088 cm^{-1}). Remarkably, the bridge and linear frequencies for CO on Rh{100} appear for the same CO surface coverages from the surface science literature without forcing the number of peaks or the peak properties (e.g., center frequency or full width at half maximum) suggesting the sizes of the facets developed during the annealing are energetically equivalent to extended Rh surfaces that can hold up to 0.75 monolayers of CO. 23-25

As noted, detailed descriptions of the deconvoluted peaks and their frequencies can be found in Tables S1-S3 and Figs S8-S10. The most important results of the deconvolutions of the FTIR spectra are the physical changes in Rh-CO binding configurations as a function of annealing temperature. These observed changes and their physical meaning regarding Rh NP development are detailed below.

First, there is a noticeable shift in frequency and an increase in intensity for the infrared bands associated with bridging CO (1850-1970 cm^{-1}) on the Rh{100} and Rh{111} surfaces 23–26



as the annealing temperature is increased. Table 1 shows these bridging carbonyls can be assigned to Rh{100} surfaces that accommodate surface coverages of $\theta_{\text{CO}}=0.20$ and $\theta_{\text{CO}}=0.35-0.40$ ML. Our FTIR results suggest Rh{100} surfaces develop as the annealing temperature is increased, which agrees with the Rh{100} surfaces observable in the post-reaction HRTEM images (Fig. 5).

Second, all deconvoluted spectra exhibit absorption peaks at 2021 cm^{-1} and 2041 cm^{-1} . The absorption peak at 2041 cm^{-1} has been observed on Rh{100} also with a surface coverage of $\theta_{\text{CO}}=0.35-0.40$ ML further suggesting the existence of Rh{100} facets. The absorption peak around 2020 cm^{-1} can be associated with CO bound in a linear configuration on Rh{100} with $\theta_{\text{CO}}=0.20$ ML thus matching the same surface coverage for the bridging CO at nominally 1887 cm^{-1} . It should be noted the peak at 2020 cm^{-1} could also be associated with the asymmetric stretch of CO bound to Rh single atoms implying the Rh CS NPs are fragmented by CO with increasing annealing temperature.

Third, the peak at 2056 cm^{-1} grows from near zero intensity for the catalyst annealed at 400°C to a dominant peak for the catalyst annealed at 575°C while the readily observable 2068 cm^{-1} peak observable at 400°C decreases to zero with increasing annealing temperature suggesting these peaks are linked to Rh crystallite development. The 2056 cm^{-1} peak is most appropriately assigned to linear bound CO on Rh{111}^{25,26} suggesting Rh{111} facets develop with increasing annealing temperature and support for the existence of these Rh{111} facets can be observed in Fig. 5. The broadening of the 2056 cm^{-1} peak on the low frequency side is ascribed to linear CO absorption peaks on Rh{100} facets in the 2041 cm^{-1} region. However, the peak at

2068 cm^{-1} cannot be assigned to CO bound to low index Rh crystal faces. Instead, a peak at 2068 cm^{-1} has been reported for CO in a linear configuration on small Rh NPs (0.9-1.5 nm).³² These small Rh NPs also exhibited an absorption peak for bridge bound CO at 1868 cm^{-1} and a discernible absorption peak is observable at 1869 cm^{-1} in the spectrum for the catalyst annealed at 400°C (Fig. S10 and Table S1). Typically, small NPs are highly stepped and the adsorption position of CO on (111) stepped surfaces such as (331) and (755) have not been widely reported. The closest report is for CO in a linear configuration on Rh(331) at 2060 cm^{-1} .³³ Therefore, it is reasonable to associate this peak at 2069 cm^{-1} with highly stepped surfaces of Rh{111}, such as {211} and {311} that would be present in irregularly shaped Rh NPs and observable in the HRTEM images in Fig. 5 of Rh/rTiO₂ exposed to RWGS reaction at temperatures less than 575°C. As noted above, this peak at 2068 cm^{-1} associated with Rh NPs (0.9-1.5 nm) and stepped Rh{111} surfaces is noteworthy because of its prominence in Fig. 7 for the catalyst annealed at 400°C while it is absent in IR spectra of catalysts annealed at 575°C. Its presence at low temperatures but disappearance at higher annealing temperature suggests the development of extended Rh structures with increasing annealing temperature. Rh nanoparticles are > 1.5 nm in diameter and/or Rh{111} facets are no longer stepped when the 2068 cm^{-1} peak disappears. The <10 cm^{-1} shift in frequency can easily be due to oxygen also bound to the Rh surfaces since CO is known to dissociate on {211}³⁴, {331} and {755} steps³⁵ and B5 and B6 defect sites associated with {111} crystal facets³⁶. The peak at 2068 cm^{-1} agrees well with a stepped or 'roughened' Rh surface as an asymmetrical shaped CO vibrational peak at 2070 cm^{-1} was observed on roughened Rh.³⁷

Finally, the peak between 2080 and 2100 cm^{-1} is comprised of two distinct peaks whose intensities shift depending on the annealing temperature. For the sample annealed at 400°C, the



asymmetry of the peak suggests the higher frequency peak is larger in intensity than the lower frequency peak while for the sample annealed at 575°C, the opposite is true. Peak deconvolution yields peaks at 2088 cm⁻¹ and 2098 cm⁻¹ for catalysts annealed at 400 and 500 °C with only the 2088 cm⁻¹ peak being present with a slightly larger full-width at half maximum (Table S1-S3) for the sample annealed at 575 °C. The peak at 2098 cm⁻¹ can be assigned to the symmetric absorption vibration of the rhodium gem-dicarbonyl since CO bound to Rh{111} has not been observed at frequencies higher than 2088.4 cm⁻¹.³⁸ Since Rh{111} facets can be observed from the truncated and non-regularly shaped octahedral Rh NPs in the HRTEM images in Fig. 5 and Fig. S8, and since it is well known CO can dissociate at stepped {111} and undercoordinated sites in fcc metals,³¹⁻³³ it is highly plausible the 2088 cm⁻¹ peak can be assigned to CO in a linear configuration on Rh{111} with O also present on the Rh{111} surface. Beyond TEM results, support for this can be inferred from the 2098 cm⁻¹:2088 cm⁻¹ peak area ratio which decreased from ~3:1 for the 0.3 wt. % Rh/rTiO₂ (CS/NP) catalyst annealed at 400°C to 0 for the catalyst annealed at 575°C. The loss of Rh-CO vibrational signature is most definitively associated with the disappearance of Rh single atoms with increasing annealing temperature. These general observations and their changes with increased annealing temperature suggest Rh is dynamic during the annealing process and evolving with increasing annealing temperature.

3.7 *Pre-annealing of Rh/rTiO₂ (CS/NP) demonstrates time and temperature determine the agnostic behavior of CO selectivity to initial Rh structure*

It is evident when heating to reaction temperature (600°C) under RWGS reaction conditions (Fig. 3) or the inclusion of a pre-anneal step prior to exposure to RWGS reactions conditions (Fig. 7), the initial CO selectivity is significantly higher because of the annealing step. There are slight



differences in the non-annealing and annealing pre-reaction protocols that we eliminate in a revised reaction protocol. In the revised procedure, two 0.3 wt. % Rh/rTiO₂ (CS/NP) catalysts were oxidized at 400°C, reduced at 200°C, and then annealed at 600°C for 1 h under N₂. However, instead of exposing the catalysts to the RWGS environment as was done for annealed catalysts (in Section 3.5), both catalysts were cooled back down to < 40°C under N₂. One of the catalyst samples was exposed to a 3:1 H₂:CO₂ gas mixture while the other remained under an inert nitrogen environment before both were simultaneously ramped to 600°C. Once at a reaction temperature of 600°C, the sample under N₂ was exposed to the 3:1 H₂:CO₂ gas mixture. The CO₂ conversion and CO selectivity as function of elapsed time can be seen in Figs. 8(b,c) respectively. In Fig. 8a, the reactor temperature, oxidation, reduction, and annealing processing steps are shown using the same color scheme as in Fig. 1.

The catalysts show very similar CO₂ conversion (Fig. 8a) and CO selectivity as a function of time once both were under RWGS reaction conditions at 600°C. The catalyst heated from < 40°C to 600°C under N₂ prior to the start of the RWGS reaction had a noticeable relative improvement of 10+% in CO₂ conversion throughout the entire time-on-stream period. Both samples have the same CO selectivity (Fig. 8b) as a function of time despite one catalyst being ramped to reaction under N₂ and the other under RWGS; the similarity in CO selectivity suggests the Rh catalyst is structurally modified during the annealing step and prior to exposure to RWGS reaction conditions. It is not clear why these catalysts started with an initial CO selectivity of > 85% rather than > 95% as was previously observed for the sample in Fig. 6b that did not undergo cooling back to < 40°C before being ramped back to 600°C. Both samples started with a substantially higher CO selectivity than the sample shown in Figure 6b that underwent a 2 h anneal at 500°C



which only had a starting CO selectivity of about 65%. It is evident the annealing of Rh at higher temperatures (600°C) improves CO selectivity. Annealing of Rh prior to RWGS reaction at 600°C for as little as 1 h and/or a RWGS reaction temperature more than 560°C yields a RWGS catalyst that is highly selective to CO and stable with respect to time.

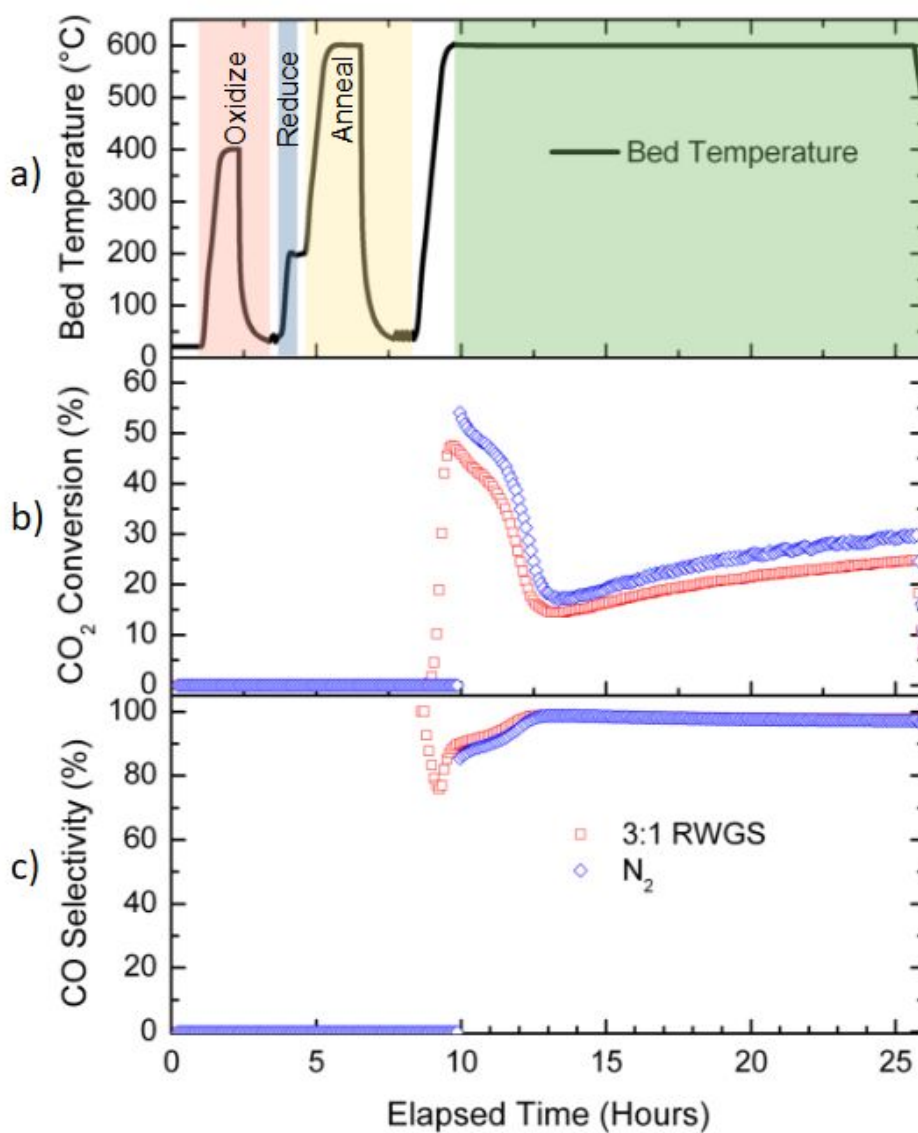


Figure 8. Influence of heat to reaction temperature environment on RWGS performance. (a) Pretreatment and reaction environment with corresponding thermal profile. (b) CO₂ conversion and (c) CO selectivity for two 0.3 wt. % Rh/rTiO₂ (CS/NP) as a function of reaction time at 600°C. Both catalysts were exposed to the same pre-reaction conditions of oxidation, reduction, annealing at 600°C for 1 h, and cooled back to <40°C before being ramped to reaction temperature. One catalyst was ramped to a reaction temperature of 600°C under a 3:1 H₂:CO₂ environment while the other catalyst was ramped to a reaction temperature of 600°C under N₂ and only exposed to 3:1 H₂:CO₂ environment after the catalyst bed reached 600°C. Both sample exhibit very similar CO₂ conversion as a function of time and almost identical CO selectivity as a function of time suggesting the changes in the Rh catalyst occurred prior to being exposed to the RWGS on ramp to reaction temperature and the RWGS environment does not affect the Rh catalytic performance on the ramp to reaction.

3.8 *Invariance of the Apparent Activation Energy for CO Formation with the Initial Rh structure Demonstrates a Common Active Site*

After 16 h time-on-stream, temporal changes in CO₂ conversion and CO selectivity are rather small, suggesting the reaction has reached steady-state and/or changes in the catalyst structure are minimal. At this point, samples were cooled via thermal loss from the insulated furnace under the 3:1 H₂:CO₂ mixture. During the reactor cool down, CO and CH₄ production rates were calculated as a function of temperature to generate an Arrhenius plot. Fig. 9a,c shows the procedure and the Arrhenius plot for a non-annealed 2.0 wt. % Rh/rTiO₂ (WI) for both CO and CH₄ over a temperature range of 390°C to 240°C. The apparent activation energy (E_a) for CO production for the 2.0 wt. % Rh/rTiO₂ (WI) is 57 kJ/mol. Duplicate measurements of the “cool down” E_a over the non-annealed 2.0 wt. % Rh/rTiO₂ (WI) showed good reproducibility.



The 0.3 wt. % Rh/rTiO₂ (CS/NP) catalyst annealed at 600°C for 1 h prior to the RWGS reaction yields a “heat-up” E_a for CO production of 60.1 kJ/mol and a “cool down” E_a for CO production of 60.8 kJ/mol both of which agree with the post reaction CS/NP average CO activation energy of 60.5 kJ/mol for the non-annealed CS/NP samples that were exposed to RWGS at 500°C for 16 h. This suggests catalysts which undergo a high temperature (600°C) pre-annealing step prior to exposure to RWGS reaction conditions obtain a Rh morphology (size and degree of ordering) similar to catalysts exposed to RWGS reaction conditions at 500°C for 16 h.

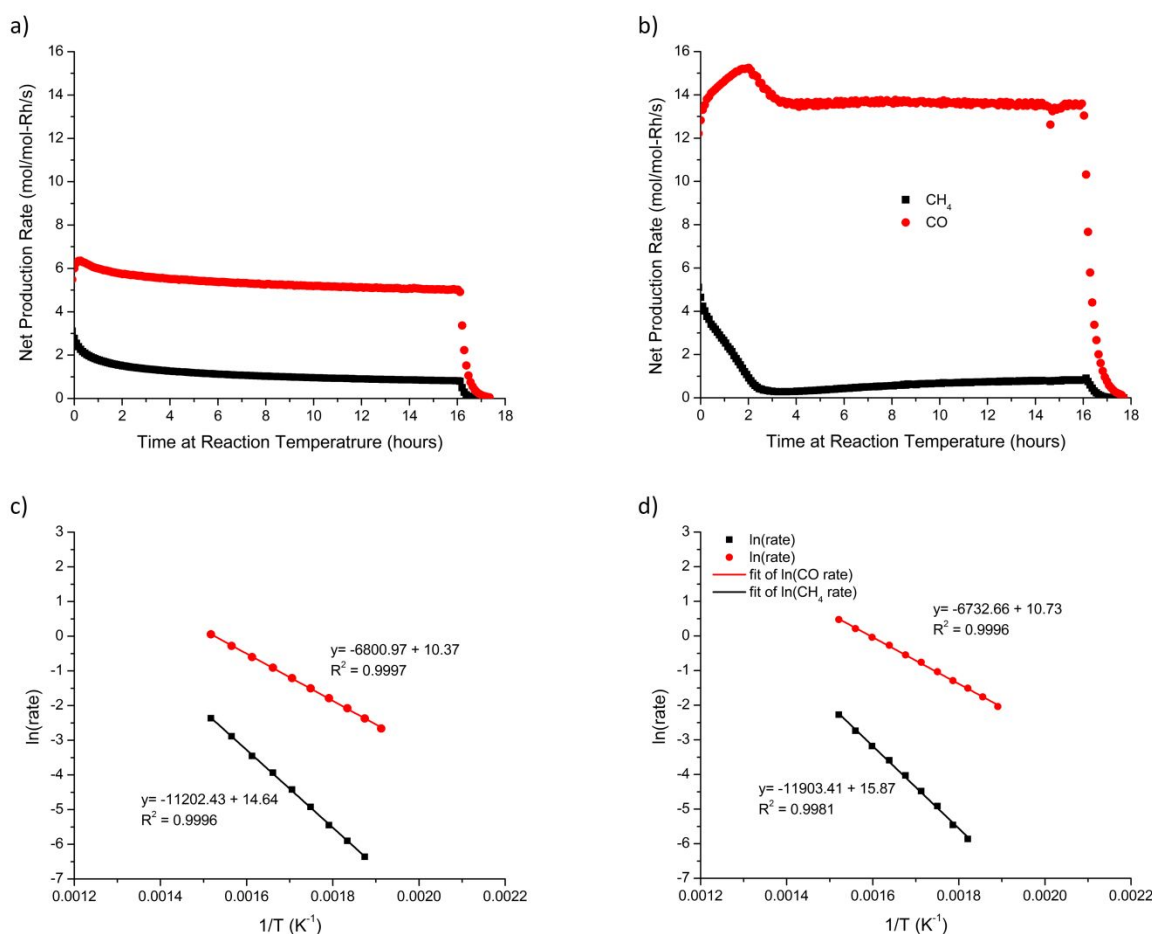


Figure 9 CO and CH₄ rates for (a) non-annealed 2.0 wt. % Rh/rTiO₂ (WI) and (b) pre-annealed (600°C, 1 h) 0.1 wt. % Rh/rTiO₂ (WI) exposed to 3:1 H₂:CO₂ mixture for 16 h and their associated cool down activation



energy plot data, (c) and (d) respectively, as function of time and temperature. The 2.0 wt. % Rh/rTiO₂ (WI) samples was run at 500°C and the 0.1 wt. % Rh/rTiO₂ (WI) sample was run at 600°C. The data used for the cool down dynamic activation energy plot can be seen in both image a) and b) for time greater than 16 h. The activation energy data plot was fit over a temperature range of nominally 240-390°C where conversion was 0.1-6%.

The fresh 0.3 wt. % Rh/rTiO₂ (CS/NP) contains NPs with a mean spherical particle size of 4.5 nm with little to no Rh speciation as single atoms (Fig. S4), while the fresh 2.0 wt. % Rh/rTiO₂ (WI) contains a mixture of single atoms and raft-like Rh NPs (Fig. S4). Upon reaction under 3:1 H₂:CO₂ at 600°C for 16 h, both catalysts contain faceted ~2 nm Rh NPs. Since these catalysts contained a large fraction of NPs in the fresh state (albeit with different structure), we conducted a 600°C anneal in N₂ for 1 h prior to the RWGS reaction on a single atom catalyst, 0.1 wt. % Rh/TiO₂ (WI). TEM analysis (Fig. 4, Fig. S5, S6, and Fig. S8) demonstrates regardless of reaction temperature, Rh NPs of ~1.8 nm in diameter are observed. However, the HRTEM analysis was unable to observe Rh single atoms, and we anticipate the population of stable Rh single atoms decreases with reaction temperature. The apparent activation energy on Rh single atoms supported on rutile TiO₂ is 101 kJ/mol²⁸, while the apparent activation energy on Rh/rTiO₂ (CS/NP) catalyst is 55-60 kJ/mol. If the 0.1 wt. % Rh/rTiO₂ (WI) catalyst still contains single atoms after reaction or pre-annealing, the measured apparent activation energy should reflect contribution from both the single atoms and ~1.8 nm NPs. We annealed the 0.1 wt. % Rh/TiO₂ (WI) catalyst at 600°C in N₂ for 1 h, cooled to < 40°C and heated (10°C/min) to 600°C under RWGS reaction conditions, followed by 16 h time-on-stream, and subsequent measurement of the E_a upon “cool-down”. Figure 9b represents the time on stream CO and CH₄ production rates of a



pre-annealed (600°C, 1h) 0.1 wt. % Rh/rTiO₂ (WI) catalyst. Upon completion of 16 h RWGS reaction, the catalyst sample was cooled down via thermal losses from the furnace. Fig. 9d is the Arrhenius plot for the annealed 0.1 wt. % Rh/rTiO₂ (WI). The value for the E_a for CO production is 57.3 kJ/mol. A second measurement on a separate bed of the annealed 0.1 wt. % Rh/rTiO₂ (WI) yielded an apparent E_a of 56 kJ/mol. The measured E_a during the cool down after 16 h time-on-stream suggests Rh NPs are responsible for CO formation even though the initial Rh structure was single atoms. The measured apparent activation energy for the RWGS reaction over Rh NP/TiO₂ (P25) has been reported to be 55 kJ/mol for a 4:1 H₂:CO₂ ratio.³⁹ The measured apparent activation energy in this work at a 3:1 H₂:CO₂ ratio is similar, but significantly lower than the value (101 kJ mol⁻¹) reported on rutile-supported single atoms of Rh.²⁸ A value of 55-60 kJ/mol for the apparent activation energy appears to be independent of the TiO₂ polymorph (rutile versus anatase).³⁹

The apparent E_a for CH₄ formation for the 2.0 wt. % Rh/rTiO₂ (WI) catalyst in a 3:1 H₂:CO₂ mixture upon cool down is ~102.8 kJ/mol (Fig. 9c), while the E_a upon cool down on the pre-annealed 0.1 wt. % Rh/rTiO₂ (WI) is 99.7 kJ/mol (Fig. 9d). Both experiments were run in duplicate, and the reproducibility between individual catalyst beds was good. These values for the apparent E_a for methane formation agree well with the reported value of Verykios and co-workers of 103 kJ/mol.³⁹ Reported E_a values for CO₂ hydrogenation to CH₄ in a 3:1 H₂:CO₂ mixture over a Rh foil^{40,41} or an inverse TiO₂/Rh foil catalyst⁴² are in the range of 130-140 kJ/mol, while a value of 100 kJ/mol was reported over an oxidized Rh foil.⁴¹ The latter value agrees well with apparent activation energy for CH₄ formation reported here and by Verykios et al.³⁹ The difference in the activation energy reported here with those from a Rh foil suggest that undercoordinated sites or



tightly bound atomic oxygen at those undercoordinated sites on the Rh nanoparticle surface may be critical for the kinetically relevant CO hydrogenation step.

Conclusions

Rh single atoms supported on rutile TiO₂ are responsible for CO formation during the reverse water gas shift reaction at low temperatures (< 400°C). As the reaction temperature is increased, the formation of CH₄ is observed which is associated with the growth of Rh nanoparticles and the formation of a Rh-TiO₂ interface, the presumed location of the active site for CH₄ formation. The Rh nanoparticles formed at low temperature are primarily disordered, and CO IR spectroscopy on these catalysts confirm significant Rh speciation (single atoms and nanoparticles). Upon heating to higher temperatures (550-600°C), the formation of methane decreases significantly even though nanoparticles and their interface with TiO₂ persist. At higher temperatures, the particles become more ordered regardless of their initial structure (single atoms or nanoparticles), and IR spectroscopy of adsorbed CO suggests the formation of CO-Rh terrace atom configurations. At a reaction temperature of 600°C under RWGS conditions (3:1 H₂:CO₂), the selectivity to CO for all Rh/rTiO₂ catalysts is >95%, and the apparent activation energy for multiple Rh/rTiO₂ with different initial Rh structures, either pre-annealed at 600°C or post RWGS (600°C for 16 h) was 55-60 kJ/mol, in good agreement with reported activation energies measured on nanoparticle Rh/rTiO₂ catalysts. The development of faceted Rh nanoparticles leads to the predominant formation of CO at higher reaction temperatures. Single atoms may persist at these higher temperatures, but the predominance of adsorbed CO associated with extended Rh surfaces and the agreement in measured apparent activation energy on nanoparticle-based Rh/rTiO₂ catalysts suggest single atoms are kinetically irrelevant at reaction



temperatures of $\sim 600^\circ\text{C}$. This study demonstrates detailed examination of catalyst activation is critical for the prediction of catalyst performance with time on stream.

Data availability

All data supporting the findings of this investigation are incorporated within the publication and the supporting information.

Author contributions

GB: conceived the initial research idea, catalyst testing, data analysis, original draft writing. XC, AK, JH, SG, LM, DZ: catalyst synthesis, catalyst characterization, discussions, writing and editing. JY, AH, MC, and RR: research supervision, writing and editing. SRB: funding acquisition, project administration, resources, supervision, writing and editing.

Conflicts of interest

There are no conflicts of interest to declare.

Acknowledgements

Selin Bac and Seunghwa Hong (UC Santa Barbara) are thanked for catalyst synthesis and helpful discussion and creation of the TOC. Jiyun Hong (SLAC) is acknowledged for help with the references. The work was supported by the Division of Chemical Sciences, Geosciences, and Biosciences, Office of Basic Energy Sciences, US Department of Energy (DOE) as part of the Accelerate Innovations in Emerging Technologies initiative, FWP 101064. This research used the Electron Microscopy and Proximal Probes Facility of the Center for Functional Nanomaterials



(CFN), which is a U.S. Department of Energy Office of Science User Facility, at Brookhaven National Laboratory under Contract No. DE-SC0012704.

Notes and references

- (1) Xie, J.; Paalanen, P. P.; van Deelen, T. W.; Weckhuysen, B. M.; Louwerson, M. J.; de Jong, K. P. Promoted Cobalt Metal Catalysts Suitable for the Production of Lower Olefins from Natural Gas. *Nature Communications* 2019 10:1 2019, 10 (1), 167-. <https://doi.org/10.1038/s41467-018-08019-7>.
- (2) Dry, M. E. The Fischer–Tropsch Process: 1950–2000. *Catal. Today* 2002, 71 (3–4), 227–241. [https://doi.org/10.1016/S0920-5861\(01\)00453-9](https://doi.org/10.1016/S0920-5861(01)00453-9).
- (3) Fischer, N.; Van Steen, E.; Claeys, M. Structure Sensitivity of the Fischer–Tropsch Activity and Selectivity on Alumina Supported Cobalt Catalysts. *J. Catal.* 2013, 299, 67–80. <https://doi.org/10.1016/J.JCAT.2012.11.013>.
- (4) Daza, Y. A.; Kuhn, J. N. CO₂ Conversion by Reverse Water Gas Shift Catalysis: Comparison of Catalysts, Mechanisms and Their Consequences for CO₂ Conversion to Liquid Fuels. *RSC Adv.* 2016, 6 (55), 49675–49691. <https://doi.org/10.1039/C6RA05414E>.
- (5) Matsubu, J. C.; Yang, V. N.; Christopher, P. Isolated Metal Active Site Concentration and Stability Control Catalytic CO₂ Reduction Selectivity. *J. Am. Chem. Soc.* 2015, 137 (8), 3076–3084. <https://doi.org/10.1021/JA5128133>.
- (6) Guan, H.; Lin, J.; Qiao, B.; Miao, S.; Wang, A. Q.; Wang, X.; Zhang, T. Enhanced Performance of Rh₁/TiO₂ Catalyst without Methanation in Water-Gas Shift Reaction. *AIChE Journal* 2017, 63 (6), 2081–2088. <https://doi.org/10.1002/AIC.15585>.
- (7) Kwak, J. H.; Kovarik, L.; Szanyi, J. CO₂ Reduction on Supported Ru/Al₂O₃ Catalysts: Cluster Size Dependence of Product Selectivity. *ACS Catal.* 2013, 3 (11), 2449–2455. <https://doi.org/10.1021/CS400381F>.
- (8) Aitbekova, A.; Wu, L.; Wrasman, C. J.; Boubnov, A.; Hoffman, A. S.; Goodman, E. D.; Bare, S. R.; Cargnello, M. Low-Temperature Restructuring of CeO₂-Supported Ru Nanoparticles Determines Selectivity in CO₂ Catalytic Reduction. *J. Am. Chem. Soc.* 2018, 140 (42), 13736–13745. <https://doi.org/10.1021/JACS.8B07615>.
- (9) Millet, M. M.; Algara-Sille, G.; Wrabetz, S.; Mazheika, A.; Girgsdies, F.; Teschner, D.; Seitz, F.; Tarasov, A.; Levchenko, S. V.; Schlögl, R.; Frei, E. Ni Single Atom Catalysts for CO₂ Activation. *J. Am. Chem. Soc.* 2019, 141 (6), 2451–2461. <https://doi.org/10.1021/JACS.8B11729>.



- (10) Schroeder, E. K.; Hong, S.; Chen, X.; Hoffman, A. S.; Chen, Z.; Khan, A.; Barber, G. D.; Bac, S.; Rioux, R. M.; Yang, J.; Tassone, C. J.; Bare, S. R.; Christopher, P. Structural Evolution and Stability of Rh/TiO₂ Catalysts under CO₂ Hydrogenation Conditions: Influence of the Initial Rh Structure. *ACS Catal.* 2025, 12133–12147. <https://doi.org/10.1021/ACSCATAL.5C02205>.
- (11) Bac, S.; Shin, D.; Hong, S.; Heinlein, J.; Khan, A.; Barber, G.; Chen, Z.; Albrechtsen, M. M.; Tassone, C.; Rioux, R. M.; Cargnello, M.; Bare, S. R.; Winther, K.; Christopher, P.; Hoffman, A. S. Quantifying Experimental Uncertainty in Catalyst Deactivation: Round Robin Testing and Implications for Machine-Learned Prediction. Submitted 2025.
- (12) Chung, P. H.; Yang, A. C.; Zhou, C.; Oh, J.; Homer, M.; Lizandara-Pueyo, C.; Li, Y.; Cargnello, M. Aqueous-Phase Synthesis of Pt and PGM-Based Nanocrystals with a Controllable Size. *Cryst. Growth Des.* 2024, 24 (24), 10413–10422. <https://doi.org/10.1021/ACS.CGD.4C01416>.
- (13) Li, L.; Wang, L. L.; Johnson, D. D.; Zhang, Z.; Sanchez, S. I.; Kang, J. H.; Nuzzo, R. G.; Wang, Q.; Frenkel, A. I.; Li, J.; Ciston, J.; Stach, E. A.; Yang, J. C. Noncrystalline-to-Crystalline Transformations in Pt Nanoparticles. *J. Am. Chem. Soc.* 2013, 135 (35), 13062–13072. https://doi.org/10.1021/JA405497P/SUPPL_FILE/JA405497P_SI_002.QT.
- (14) Eads, C. N.; Boscoboinik, J. A.; Head, A. R.; Hunt, A.; Waluyo, I.; Stacchiola, D. J.; Tenney, S. A. Enhanced Catalysis under 2D Silica: A CO Oxidation Study. *Angewandte Chemie - International Edition* 2021, 60 (19), 10888–10894. <https://doi.org/10.1002/ANIE.202013801>.
- (15) Granqvist, C. G.; Buhrman, R. A. Size Distributions for Supported Metal Catalysts: Coalescence Growth versus Ostwald Ripening. *J. Catal.* 1976, 42 (3), 477–479. [https://doi.org/10.1016/0021-9517\(76\)90125-1](https://doi.org/10.1016/0021-9517(76)90125-1).
- (16) Hansen, T. W.; Delariva, A. T.; Challa, S. R.; Datye, A. K. Sintering of Catalytic Nanoparticles: Particle Migration or Ostwald Ripening? *Acc. Chem. Res.* 2013, 46 (8), 1720–1730. <https://doi.org/10.1021/AR3002427>.
- (17) Yin, P.; Hu, S.; Qian, K.; Wei, Z.; Zhang, L. Le; Lin, Y.; Huang, W.; Xiong, H.; Li, W. X.; Liang, H. W. Quantification of Critical Particle Distance for Mitigating Catalyst Sintering. *Nature Communications* 2021 12:1 2021, 12 (1), 4865-. <https://doi.org/10.1038/s41467-021-25116-2>.
- (18) Li, Y.; Zakharov, D.; Zhao, S.; Tappero, R.; Jung, U.; Elsen, A.; Baumann, P.; Nuzzo, R. G.; Stach, E. A.; Frenkel, A. I. Complex Structural Dynamics of Nanocatalysts Revealed in Operando Conditions by Correlated Imaging and Spectroscopy Probes. *Nature Communications* 2015 6:1 2015, 6 (1), 7583-. <https://doi.org/10.1038/ncomms8583>.



- (19) Yu, W.; Yue, S.; Yang, M.; Hashimoto, M.; Liu, P.; Zhu, L.; Xie, W.; Jones, T.; Willinger, M.; Huang, X. Operando TEM Study of a Working Copper Catalyst during Ethylene Oxidation. *Nature Communications* 2025 16:1 2025, 16 (1), 2029-. <https://doi.org/10.1038/s41467-025-57418-0>.
- (20) Hoffman, A. J.; Asokan, C.; Gadinis, N.; Kravchenko, P.; Getsoian, A. "Bean"; Christopher, P.; Hibbitts, D. Theoretical and Experimental Characterization of Adsorbed CO and NO on γ -Al₂O₃-Supported Rh Nanoparticles. *The Journal of Physical Chemistry C* 2021, 125 (36), 19733–19755. <https://doi.org/10.1021/ACS.JPCC.1C05160>.
- (21) Hoffman, A. J.; Asokan, C.; Gadinis, N.; Schroeder, E.; Zakem, G.; Nystrom, S. V.; Getsoian, A. B.; Christopher, P.; Hibbitts, D. Experimental and Theoretical Characterization of Rh Single Atoms Supported on γ -Al₂O₃ with Varying Hydroxyl Contents during NO Reduction by CO. *ACS Catal.* 2022, 12 (19), 11697–11715. <https://doi.org/10.1021/ACSCATAL.2C02813>.
- (22) Asokan, C.; Thang, H. V.; Pacchioni, G.; Christopher, P. Reductant Composition Influences the Coordination of Atomically Dispersed Rh on Anatase TiO₂. *Catal. Sci. Technol.* 2020, 10 (6), 1597–1601. <https://doi.org/10.1039/D0CY00146E>.
- (23) Leung, L. W. H.; He, J. W.; Goodman, D. W. Adsorption of CO on Rh(100) Studied by Infrared Reflection–Absorption Spectroscopy. *J. Chem. Phys.* 1990, 93 (11), 8328–8336. <https://doi.org/10.1063/1.459316>.
- (24) De Jong, A. M.; Niemantsverdriet, J. W. The Adsorption of CO on Rh(100): Reflection Absorption Infrared Spectroscopy, Low Energy Electron Diffraction, and Thermal Desorption Spectroscopy. *J. Chem. Phys.* 1994, 101 (11), 10126–10133. <https://doi.org/10.1063/1.468001>.
- (25) Linke, R.; Curulla, D.; Hopstaken, M. J. P.; Niemantsverdriet, J. W.; Curulla, D.; Hopstaken, M. J. P.; Niemantsverdriet, J. W. CO/Rh(111): Vibrational Frequency Shifts and Lateral Interactions in Adsorbate Layers. *J. Chem. Phys.* 2001, 115 (17), 8209–8216. <https://doi.org/10.1063/1.1355767>.
- (26) Krenn, G.; Bako, I.; Schennach, R. CO Adsorption and CO and O Coadsorption on Rh(111) Studied by Reflection Absorption Infrared Spectroscopy and Density Functional Theory. *Journal of Chemical Physics* 2006, 124 (14), 144703. <https://doi.org/10.1063/1.2184308/929455>.
- (27) Dubois, L. H.; Somorjai, G. A. The Chemisorption of CO and CO₂ on Rh(111) Studied by High Resolution Electron Energy Loss Spectroscopy. *Surf. Sci.* 1980, 91 (2–3), 514–532. [https://doi.org/10.1016/0039-6028\(80\)90348-9](https://doi.org/10.1016/0039-6028(80)90348-9).
- (28) Tang, Y.; Asokan, C.; Xu, M.; Graham, G. W.; Pan, X.; Christopher, P.; Li, J.; Sautet, P. Rh Single Atoms on TiO₂ Dynamically Respond to Reaction Conditions by Adapting Their Site.



Nature Communications 2019 10:1 2019, 10 (1), 4488-. <https://doi.org/10.1038/s41467-019-12461-6>.

- (29) Asokan, C.; Xu, M.; Dai, S.; Pan, X.; Christopher, P. Synthesis of Atomically Dispersed Rh Catalysts on Oxide Supports via Strong Electrostatic Adsorption and Characterization by Cryogenic Infrared Spectroscopy. *The Journal of Physical Chemistry C* 2022, 126 (44), 18704–18715. <https://doi.org/10.1021/ACS.JPCC.2C05426>.
- (30) Swart, I.; De Groot, F. M. F.; Weckhuysen, B. M.; Rayner, D. M.; Meijer, G.; Fielicke, A. The Effect of Charge on CO Binding in Rhodium Carbonyls: From Bridging to Terminal CO. *J. Am. Chem. Soc.* 2008, 130 (7), 2126–2127. <https://doi.org/10.1021/JA0772795>.
- (31) Meunier, F. C. Relevance of IR Spectroscopy of Adsorbed CO for the Characterization of Heterogeneous Catalysts Containing Isolated Atoms. *The Journal of Physical Chemistry C* 2021, 125 (40), 21810–21823. <https://doi.org/10.1021/ACS.JPCC.1C06784>.
- (32) Albrahim, M. A.; Shrotri, A.; Unocic, R. R.; Hoffman, A. S.; Bare, S. R.; Karim, A. M. Size-Dependent Dispersion of Rhodium Clusters into Isolated Single Atoms at Low Temperature and the Consequences for CO Oxidation Activity. *Angewandte Chemie - International Edition* 2023, 62 (44), e202308002. <https://doi.org/10.1002/ANIE.202308002>.
- (33) Wang, Z.; Pang, X. & Wang, R. Adsorption of CO Molecules on Rh Low Index and (331) Stepped Surfaces. *Chinese Science Bulletin* 2004, 49 (1), 101012–101019. <https://doi.org/10.1360/03wb0127>.
- (34) Degerman, D.; Shipilin, M.; Lömker, P.; Goodwin, C. M.; Gericke, S. M.; Hejral, U.; Gladh, J.; Wang, H. Y.; Schlueter, C.; Nilsson, A.; Amann, P. Operando Observation of Oxygenated Intermediates during CO Hydrogenation on Rh Single Crystals. *J. Am. Chem. Soc.* 2022, 144 (16), 7038–7042. <https://doi.org/10.1021/JACS.2C00300>.
- (35) Castner, D. G.; Somorjai, G. A. LEED and Thermal Desorption Studies of Small Molecules (H₂, O₂, CO, CO₂, NO, C₂H₄, C₂H₂ and C) Chemisorbed on the Stepped Rhodium (755) and (331) Surfaces. *Surf. Sci.* 1979, 83 (1), 60–82. [https://doi.org/10.1016/0039-6028\(79\)90480-1](https://doi.org/10.1016/0039-6028(79)90480-1).
- (36) Ligthart, D. A. J. M.; Pilot, I. A. W.; Almutairi, A. A. H.; Hensen, E. J. M. Identification of Step-Edge Sites on Rh Nanoparticles for Facile CO Dissociation. *Catal. Commun.* 2016, 77, 5–8. <https://doi.org/10.1016/J.CATCOM.2016.01.006>.
- (37) He, J. W.; Kuhn, W. K.; Leung, L. W. H.; Goodman, D. W. Infrared Vibrational Studies of CO Adsorption on Ultrathin Cu Films on a Rh(100) Surface. *J. Chem. Phys.* 1990, 93 (10), 7463–7470. <https://doi.org/10.1063/1.459420>.



- (38) Jamka, E. A.; Gillum, M. Z.; Grytsyshyn-Giger, C. N.; Lewis, F. J.; Killelea, D. R. Temperature-Resolved Surface Infrared Spectroscopy of CO on Rh(111) and (2 × 1)-O/Rh(111). *Journal of Vacuum Science & Technology A* 2022, 40 (4), 43209. <https://doi.org/10.1116/6.0001932/2846457>.
- (39) Zhang, Z.; Kladi, A.; Verykios, X. E. Effects of Carrier Doping on Kinetic Parameters of CO₂ Hydrogenation on Supported Rhodium Catalysts. *J. Catal.* 1994, 148 (2), 737–747. <https://doi.org/10.1006/JCAT.1994.1260>.
- (40) Sexton, B. A.; Somorjai, G. A. The Hydrogenation of CO and CO₂ over Polycrystalline Rhodium: Correlation of Surface Composition, Kinetics and Product Distributions. *J. Catal.* 1977, 46 (2), 167–189. [https://doi.org/10.1016/0021-9517\(77\)90198-1](https://doi.org/10.1016/0021-9517(77)90198-1).
- (41) Castner, D. G.; Blackadar, R. L.; Somorjai, G. A. CO Hydrogenation over Clean and Oxidized Rhodium Foil and Single Crystal Catalysts. Correlations of Catalyst Activity, Selectivity, and Surface Composition. *J. Catal.* 1980, 66 (2), 257–266. [https://doi.org/10.1016/0021-9517\(80\)90030-5](https://doi.org/10.1016/0021-9517(80)90030-5).
- (42) Williams, K. J.; Boffa, A. B.; Salmeron, M.; Bell, A. T.; Somorjai, G. A. The Kinetics of CO₂ Hydrogenation on a Rh Foil Promoted by Titania Overlayers. *Catal. Letters* 1991, 9 (5–6), 415–426. <https://doi.org/10.1007/BF00764834>.



Data availability

All data supporting the findings of this investigation are incorporated within the publication and the supporting information.

